NEUROPHYSIOLOGY

Distorted neurocomputation by a small number of extra-large spines in psychiatric disorders

Kisho Obi-Nagata[1,2], Norimitsu Suzuki[1], Ryuhei Miyake[1], Matthew L. MacDonald[3], Kenneth N. Fish[3], Katsuya Ozawa[1], Kenichiro Nagahama[4,5], Tsukasa Okimura[6], Shoji Tanaka[7], Masanobu Kano[4,5], Yugo Fukazawa[8], Robert A. Sweet[3], Akiko Hayashi-Takagi[1,2]*

Human genetics strongly support the involvement of synaptopathy in psychiatric disorders. However, trans-scale causality linking synapse pathology to behavioral changes is lacking. To address this question, we examined the effects of synaptic inputs on dendrites, cells, and behaviors of mice with knockdown of SETD1A and DISC1, which are validated animal models of schizophrenia. Both models exhibited an overrepresentation of extra-large (XL) synapses, which evoked supralinear dendritic and somatic integration, resulting in increased neuronal firing. The probability of XL spines correlated negatively with working memory, and the optical prevention of XL spine generation restored working memory impairment. Furthermore, XL synapses were more abundant in the postmortem brains of patients with schizophrenia than in those of matched controls. Our findings suggest that working memory performance, a pivotal aspect of psychiatric symptoms, is shaped by distorted dendritic and somatic integration via XL spines.

INTRODUCTION

Mental disorders, such as schizophrenia (SZ), and neurodevelopmental disorders (NDDs), are leading causes of the global health burden. Although these two disorders are distinct, they share a developmental origin and several clinical features, which are associated with alterations in neural connectivity (*1*). For example, working memory deficit is one of the most prevalent symptoms of SZ (*2*), which correlates with higher functional connectivity within the default mode network, especially the medial prefrontal cortex (PFC) (*3*). Moreover, cerebral cortical–thalamic hyperconnectivity is related to impaired working memory (WM) performance and predicts poorer clinical outcomes in patients with SZ (*4*, *5*). In regard to autism spectrum disorder (ASD), which is a major type of NDD, higher functional connectivity predicts greater symptom severity (*6*). Despite such accumulating evidence, the mechanisms underlying this distorted connectivity at the synaptic and cellular levels remain elusive, blurring the therapeutic targets for these disorders.

Cutting-edge genomic research has demonstrated that disease-relevant genetic variants are shared across these two disorders (*7*–*11*), and these variants accumulate considerably in the excitatory synaptic network (*12*–*16*). Most neocortical excitatory synapses are located on dendritic spines (*17*, *18*), and pathological studies using postmortem brains have revealed a selective loss of smaller spines and a shift in spine volume distributions toward larger sizes in SZ individuals (*19*). However, because of the limitations of functional studies of synapses in humans, the causality and pathological mechanisms of spine abnormalities in mental disorders remain unclear.

Thus, we focused on two disease-related genetic variations with large effect sizes. One is a loss of function (LoF) of *SETD1A*, which encodes the active domain of H3K4 methyltransferase; it is currently the only gene in which LoF variants are replicated in SZ and NDD patients with genome-wide significance (*11*, *20*). The second is an LoF variant of *DISC1*, in which a chromosomal translocation was found to segregate various mental disorders in a large Scottish family (*21*). Whole-genome sequencing of NDD individuals enabled the identification of an exonic deletion in the *DISC1* gene, which was not detected in 15,000 control individuals (*22*). We aimed to elucidate the relationship among synaptic inputs, neuronal computation, and working memory performance of *SETD1A* hetero-knockout (hKO) (*23*) and *DISC1* conditional knockdown (cKD) mice (*24*, *25*) using two-photon glutamate uncaging of single spines (*26*), patch-clamp electrophysiological analyses, biophysical simulation (*27*), behavioral analyses, and optical shrinkage of extra-large (XL) spines (*28*). Furthermore, we performed the structural analysis of spines in the postmortem brains of patients with SZ and matched controls to determine the relevance of synapse pathology in human patients.

RESULTS

XL spines are increased in two SZ mouse models

Morphological analysis revealed that both *SETD1A* hKO (*23*) and *DISC1* cKD (*25*) mice (table S1) had markedly larger spines than controls in layers II/III PFC pyramidal neurons after postnatal day 60 (P60) (Fig. 1, A and B). As an index of the strength of the excitatory synapse, we used the diameter of the spine head, the rationale for which is described in fig. S1. To examine whether larger spines have distinct properties, we experimentally measured the

[1]Laboratory for Multi-scale Biological Psychiatry, Center for Brain Science, RIKEN, 2-1 Hirosawa, Wako City, Saitama 351-0106, Japan. [2]Gunma University Graduate School of Medicine, Maebashi City, Gunma 371-8512, Japan. [3]Departments of Psychiatry, Neurology, Statistics, and Neurobiology, Translational Neuroscience Program, University of Pittsburgh, School of Medicine, Pittsburgh, PA 15213, USA. [4]Department of Neurophysiology, Graduate School of Medicine, The University of Tokyo, Tokyo 113-0033, Japan. [5]International Research Center for Neurointelligence (WPI-IRCN), The University of Tokyo, Tokyo, Japan. [6]Medical Institute of Developmental Disabilities Research, Showa University, Tokyo 157-8577, Japan. [7]Department of Information and Communication Sciences, Sophia University, 7-1 Kioicho, Chiyoda-ku, Tokyo 102-8554, Japan. [8]Division of Brain Structure and Function, Faculty of Medical Science, University of Fukui, Yoshida, Fukui, 910-1193, Japan.
*Corresponding author. Email: akiko.hayashi-takagi@riken.jp

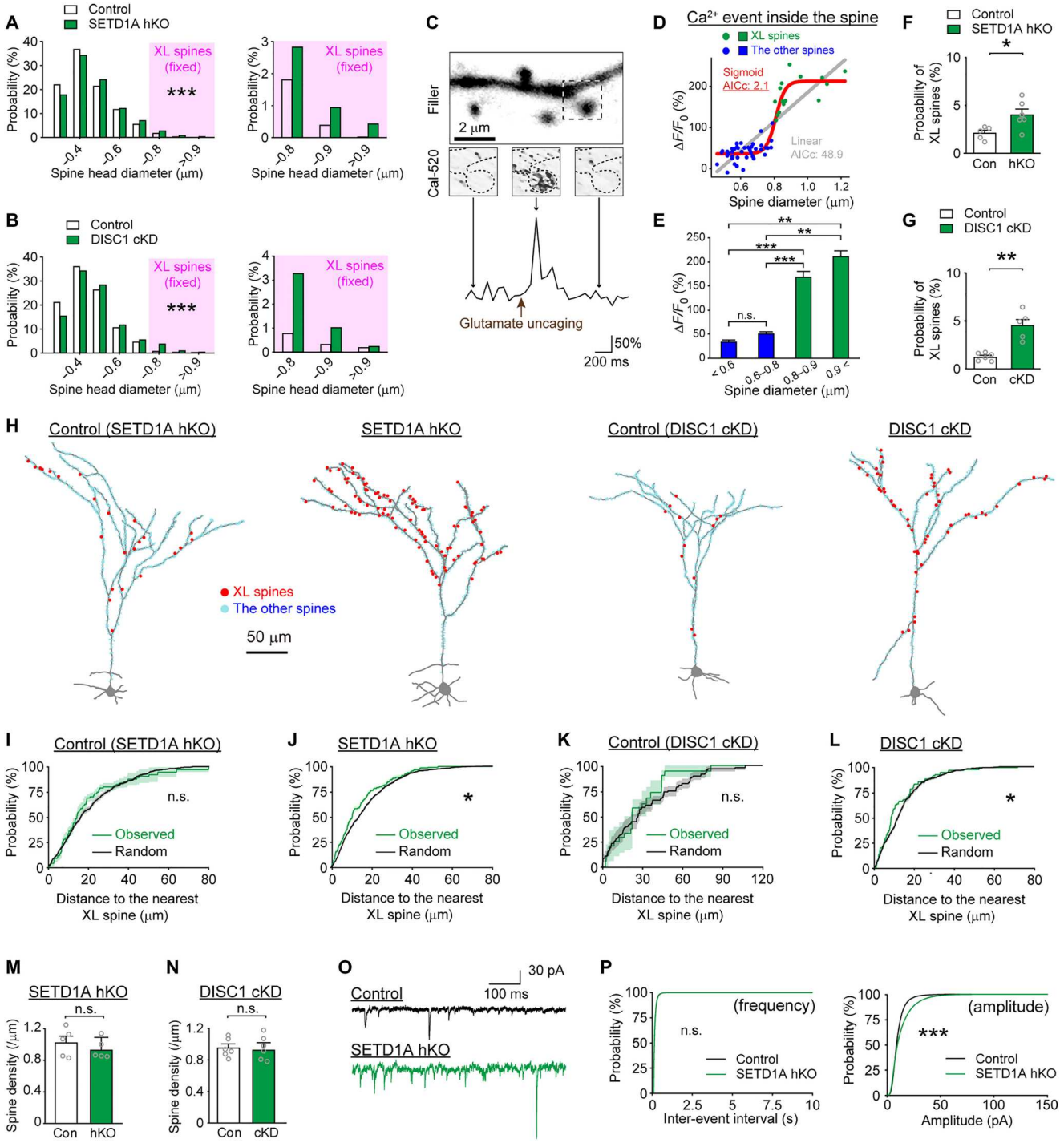

Fig. 1. Overrepresentation of XL spines in two SZ mouse models. (**A** and **B**) Histograms of pyramidal neuron spine head diameters in layers II/III of the PFC in *SETD1A* hKO (A) and *DISC1* cKD mice (B) at P60. $n = 6$ dendrites per condition. (**C** to **E**) Intra-spine Ca^{2+} events, as indicated by the fluorescence change of Cal-520 dye upon single-spine glutamate uncaging. A representative image is shown (C). Relationship between spine diameter and integrals of the intra-spine Ca^{2+} event fitted a sigmoidal function (red approximate line) rather than a linear function (gray approximate line). Fitting was supported by the corrected Akaike information criterion (AICc), in which the model with the lowest AICc is considered to be most appropriate (D). Large intra-spine Ca^{2+} event in XL spines (E). (**F** and **G**) Probability of XL spines in (A) and (B). (**H**) Pyramidal cells reconstructed from high-magnification images. Control (SETD1A hKO) and control (*DISC1* cKD) indicate wild-type littermate of *SETD1A* hKO and wild-type with control short hairpin RNA, respectively. XL spines are represented by red dots. (**I** to **L**) Significant clustering of XL spines in the experimentally observed cells ($n = 9$) of *SETD1A* hKO (J) and *DISC1* cKD mice (L), as revealed by comparisons with randomly distributed virtual cells ($n = 45$). No clustering of XL spines was observed in control mice (I) and (J). (**M** and **N**) Spine densities of *SETD1A* hKO (M) and *DISC1* cKD mice (N). (**O** and **P**) miniature excitatory postsynaptic currents in acute slices of the PFC. Representative traces (O), cumulative frequency plots (P), and amplitudes (P) of control and *SETD1A* hKO mice. $n = 13$ cells per condition. See also table S1 for measurements and statics. $^*P < 0.05$, $^{**}P < 0.01$, $^{***}P < 0.001$. n.s., not significant.

intra-spine Ca^{2+} response to synaptic inputs (Fig. 1C). The amplitude of the intra-spine Ca^{2+} was well described by the steep sigmoidal function with an inflection point at 0.8 μm in the spine diameter (Fig. 1D), and the Ca^{2+} response of the XL spines was markedly increased relative to other normal-size spines (Fig. 1E). We defined spines in which the diameter was larger than 0.8 μm as XL spines [>0.7 μm in fixed samples, considering shrinkage due to the fixative (*29*)]. Both *SETD1A* hKO and *DISC1* cKD models had significantly higher numbers of XL spines than control mice (Fig. 1, F and G) despite identical spine densities (Fig. 1, M and N) and neuronal morphologies (fig. S2, A and B) as those of control neurons. To exclude the possibility of off-target effects of RNAi against the *DISC1* gene, we also quantified spine size in another *DISC1* model that lacks exons 2 and 3 of the *DISC1* gene, resulting in the KD of some isoforms of *DISC1* (*30*). Because the probability of XL spines was significantly increased in this model compared to the littermate control mice, we concluded that the generation of XL spines was due to the LoF of *DISC1* (fig. S2, C and D). XL spines in control mice did not cluster (Fig. 1, I and K), while XL spines in both disease models formed clusters, most of which were localized within 40 μm (Fig. 1, J and L) in the distal dendrites (fig. S2E). Because dendritic computation units, which supralinearly modulate synaptic inputs, are predicted to be within ~40 μm (*31*), the clusters of XL spines could potentially function as dendritic computation units. The measurement of miniature excitatory postsynaptic currents (mEPSCs) demonstrated that the cumulative distribution of mEPSC amplitudes was rightward-shifted in both models, suggesting the presence of very large synaptic inputs ($P < 0.001$ for *SETD1A* hKO mice; $P < 0.001$ for *DISC1* cKD mice) (Fig. 1, O and P, and fig. S4, A and B). Consistently, electron microscopic (EM) analysis revealed that putative XL spines (>0.3 μm^3) in *DISC1* cKD mice formed large postsynaptic densities (PSDs) apposed to active zones with synaptic vesicle accumulations in axon terminals as were in those of control mice (fig. S3). Large spines of control mice, although less common, had qualitatively comparable properties to large spines of *DISC1* cKD mice. Large spines in both genotypes exhibited a significant correlation between spine volume and PSD area ($r_s = 0.69$, $P < 0.001$ for *DISC1* cKD mice; $r_s = 0.60$, $P < 0.01$ for control mice; fig. S3) and comparable cross section of the spine neck ($P = 0.65$; fig. S3). The frequency of mEPSCs was not altered ($P = 0.99$ for *SETD1A* hKO mice; $P = 0.38$ for *DISC1* cKD mice), which was consistent with the spine density analysis (Fig. 1, M and N). Intrinsic dendritic and neuronal excitability was identical between the control and SZ model mice (fig. S4, C to X), which suggested that the larger amplitudes of the mEPSCs in both model neurons were derived from extremely strong functional synapses.

XL spines amplify supralinear dendritic summation

To examine the (patho)physiological function of XL spines, we established a single-spine activation protocol using two-photon uncaging of 4-methoxy-7-nitroindolinyl (MNI)–glutamate (*26*) and the simultaneous measurement of dendritic Ca^{2+} responses and the somatic membrane potential upon spine activation. Previous studies demonstrated that excitatory postsynaptic potentials (EPSPs) upon the coactivation of eight typical-sized spines on a single dendritic branch are supralinearly summated, evoking an action potential (AP) (*32*). This phenomenon was replicated in our protocol (fig. S5, C to G). Notably, coactivation of only three to four XL spines was sufficient to trigger an AP (Fig. 2, A to E), although the arithmetic sum of their EPSPs and spine diameters was smaller than those of eight non-XL spines (i.e., the "other" spines) (Fig. 2C). Pooled data revealed that the activation of XL spines significantly amplified supralinear summation, such that the EPSP measured at the soma was larger than the arithmetic sum of EPSPs ($P < 0.05$ for *SETD1A* hKO mice, $P < 0.01$ for *DISC1* cKD mice; Fig. 2, D and E), which suggested that a smaller number of spines can evoke supralinear amplification when XL spines receive synaptic inputs. The supralinear dendritic summation by XL spines was similarly observed in basal and apical dendrites of layer II/III neurons and an apical dendrite of layer V neurons in the prelimbic and secondary motor cortices (fig. S6, A to C), which suggested that the XL spine–evoked AP is universal in the neocortex. XL spines are extremely sparse in control mice, but once we managed to locate the clustered XL spines in the control neurons, an identical supralinear synaptic summation was observed (fig. S6, D to K).

Supralinear summation by XL spines is NMDAR-dependent

To elucidate the molecular mechanism of supralinear synaptic summation by XL spines, we conducted time-series line-scan imaging of an XL spine and the adjacent dendritic shaft during glutamate uncaging (Fig. 2F). Evoked Ca^{2+} events originated at the head of the XL spine and subsequently penetrated the dendritic shaft (Fig. 2G), eventually evoking an AP. Blockade of voltage-dependent Na^+ channels did not affect synaptic or dendritic events; however, it completely abolished APs (Fig. 2, H to K). By contrast, the synaptic event and resultant AP were completely blocked by D-AP5, a blocker of the *N*-methyl-D-aspartate (NMDA) receptor (NMDAR), but were not affected by cadmium, a blocker of voltage-dependent Ca^{2+} channels (VDCCs) (Fig. 2, H to K). Considering that VDCCs are crucial contributors to active dendritic processing, such as dendritic spikes (*33*), we noted that the depolarization of XL spines and subsequent passive propagation is sufficient for AP generation and that dendritic spikes are dispensable during this process. To examine how XL spines generate APs without VDCC-dependent Ca^{2+} spikes, we performed biophysics simulations in the NEURON platform (*27*), whereby voltage changes were simulated at the spine, apical tuft, main bifurcation, and soma (Fig. 3A). We used parameters from our single-spine EPSC experiments (fig. S7 and table S2). In line with the experimental data (fig. S5, C to G), the simulation data replicated the generation of the AP via the coactivation of eight typical-sized spines; the AP was inhibited when we set the conductance of the VDCCs (g_{Ca}) to zero (Fig. 3B). By contrast, even with g_{Ca} at zero, the activation of three XL spines reliably induced APs (Fig. 3B), which was consistent with the experimental data (Fig. 2, I to K). During voltage propagation along the apical tuft and main bifurcation, the contributions of g_{Ca} to the elevation of the membrane potential were identical for XL spines and typical-sized spines (Fig. 3, C to E), which suggested that synaptic depolarization inside XL spines, but not active dendritic processing, is a determining factor for AP generation by XL spines.

Given the robust effect of XL spines, we next characterized the effect of a single XL spine. The NEURON simulation demonstrated that the amplitude of synaptic depolarization enhanced with the increase in spine diameter (fig. S8A). The duration of the intra-spine EPSP in XL spines was markedly longer than that in typical-sized spines (fig. S8B), thus enhancing the probability of temporal

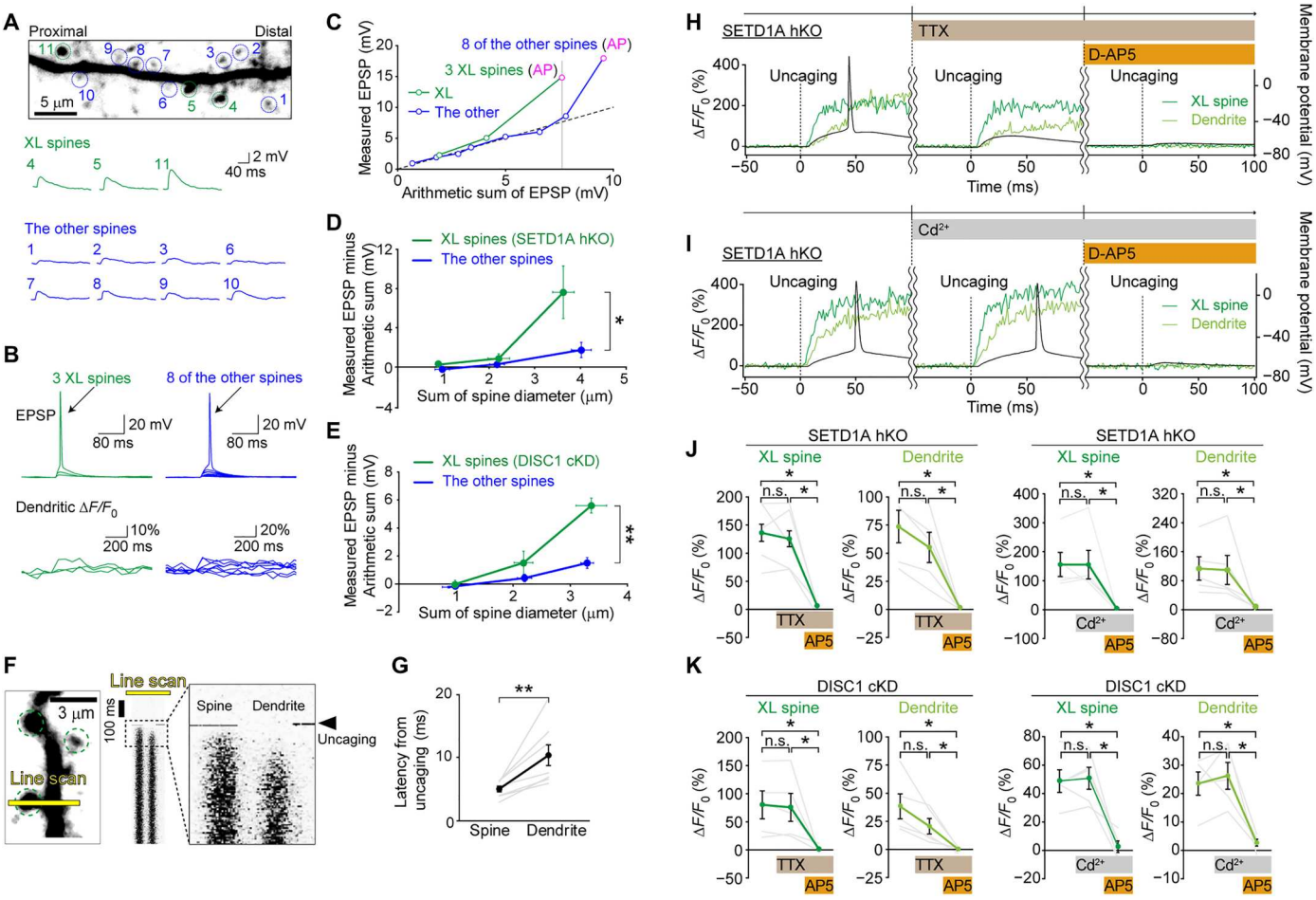

Fig. 2. XL spines amplify supralinear synaptic summation. (**A**) Two-photon image of a representative dendritic tuft with XL and normal spines. Green and blue color codes indicate the uncaging of XL spine(s) and normal spines, respectively. XL spines (spines #4, #5, and #11 diameter average = 1.08 ± 0.03 μm) and normal spines (spine #1, #2, #3, #6, #7, #8, #9, and #10 diameter average = 0.70 ± 0.02 μm). (**B**) EPSPs were measured at the soma, and dendritic $\Delta F/F_0$ represents Ca^{2+} transients in the dendritic branch adjacent to the stimulated spines of the same neuron. (**C**) Relationship between total evoked EPSP and the sum of single-spine–evoked EPSPs. (**D**) Supralinear synaptic integration in *SETD1A* hKO mice. The *y* axis indicates the degree of supralinearity, which was calculated by the difference between measured EPSPs and the sum of EPSPs. $n = 3$ cells per condition; XL spines 1.02 ± 0.03 μm ($n = 23$ spines); normal spines 0.67 ± 0.02 μm ($n = 12$ spines). (**E**) Supralinear synaptic integration in *DISC1* cKD mice. $n = 5$ cells per condition; XL spines 1.02 ± 0.03 μm ($n = 19$ spines); normal spines 0.67 ± 0.02 μm ($n = 33$ spines). (**F**) Time-series line-scan Ca^{2+} imaging of a stimulated XL spine and its parent dendrite. (**G**) Latencies of synaptic and dendritic Ca^{2+} events after glutamate uncaging. (**H** and **I**) Line-scan Ca^{2+} imaging of a stimulated XL spine and its parent dendrite upon glutamate uncaging in the presence of tetrodotoxin (TTX) (1 μM), Cd^{2+} (300 μM), and D-AP5 (250 μM). (**J** and **K**) Amplitudes of $\Delta F/F_0$ in a stimulated XL spine and its parent dendrite in *SETD1A* hKO (J) and *DISC1* cKD mice (K) before and after the application of TTX, Cd^{2+}, and D-AP5. *$P < 0.05$, **$P < 0.01$. See also table S1 for measures and statistics.

summation. These results prompted us to directly demonstrate whether the activation of a single XL spine can evoke an AP, and we found one case in which stimulation of one XL spine (but not neighboring typical-sized spines) reliably evoked an AP (Fig. 3F). Intra-spine EPSPs in XL spines are predominantly shaped by NMDAR conductance but not VDCC or voltage-gated Na^+ channels (fig. S8, C to E).

Enhanced neuronal firing and unstable circuit dynamism in SZ model mice

Given the substantial effect of XL spines, we next examined neuronal firing and connectivity in the SZ models. In vivo cell-attached recordings in the PFC revealed that the spontaneous firing of SZ model neurons was significantly enhanced ($P < 0.001$ for *SETD1A* hKO mice, $P < 0.001$ for *DISC1* cKD mice; Fig. 4, A to D).

To gain insight into the contribution of XL spines to network dynamics in vivo, we used computational approaches. A series of prior studies using single-neuron recordings from task-performing monkeys have established a link between the working memory process and information-specific persistent neuronal activity in the PFC (*34*). Using a biologically plausible model that reproduces this phenomenon (*35*), we evaluated the effect of synaptic inputs from XL spines on network dynamics. The leaky integrate-and-fire model was used to construct a local circuit model of the PFC to simulate the effect of each receptor (*36*). The model was composed of 144 pyramidal neurons and 36 interneurons. Both types of neurons were in a single compartment of the leaky integrate-

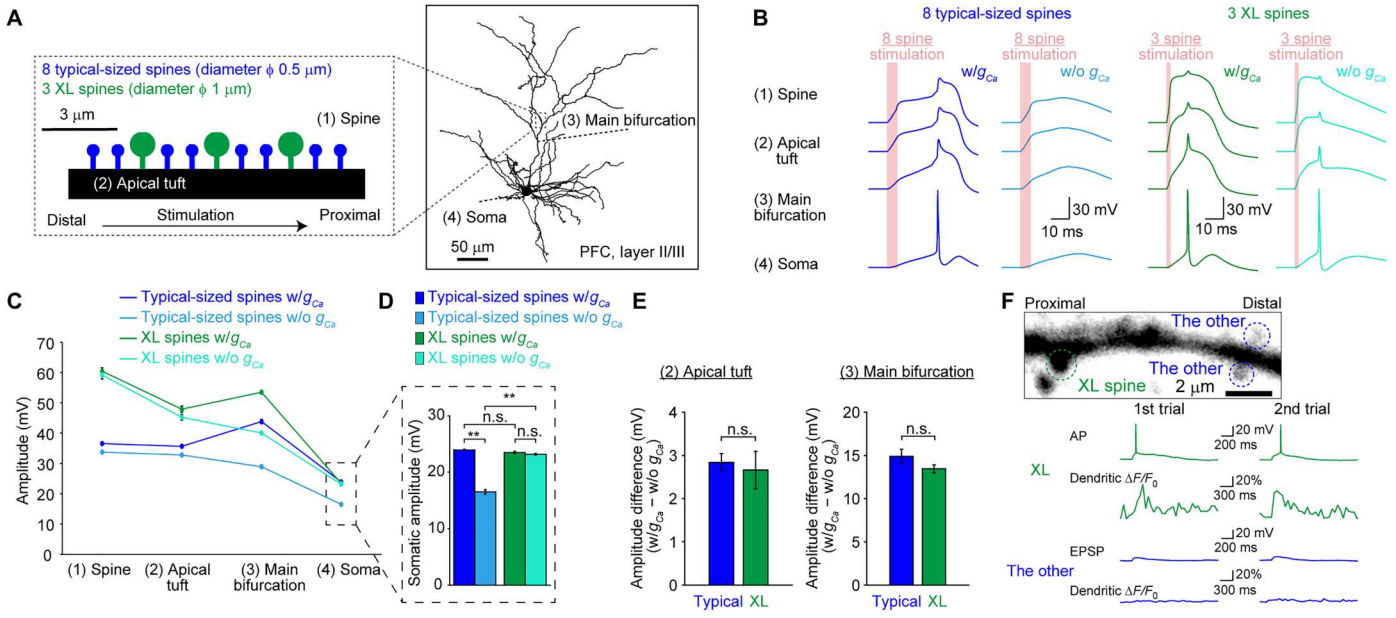

Fig. 3. NMDAR-dependent supralinear summation by XL spines and unstable circuit dynamism in SZ models. (**A**) Simulated sites for determining membrane potentials using the NEURON platform (1) inside the spine, (2) apical tuft, (3) main bifurcation, and (4) soma. (**B**) Membrane potentials after the coactivation of spines (eight normal-sized spines and three XL spines) at each segment were stimulated, and differences between intact (w/ g_{Ca}) and zero (w/o g_{Ca}) conductance of VDCCs were compared. (**C** and **D**) Elevation of membrane potential from baseline upon activation of three XL spines or eight typical-sized spines (C). Somatic membrane potential of XL spine and normal-sized spine synaptic depolarization (D). (**E**) Difference in membrane potentials between intact and zero g_{Ca} in the dendrite. $n = 8$ dendrites. Parameters used in the NEURON simulation are available in table S2 (*57*, *58*). (**F**) Induction of AP by a single XL spine but not its neighboring normal-sized spines. Dendritic Ca^{2+} transients and somatic EPSPs upon glutamate uncaging are shown. $^{**}P < 0.01$. See also table S1 for measures and statics.

and-fire model and had NMDARs, AMPA receptors (AMPARs), and other ion channels (Fig. 4E). The model was applied using the experimentally measured NMDA- and AMPA-EPSC values of XL spines (fig. S7). As a working memory task, a cue signal input was presented to the pyramidal neurons during the cue period (red rectangle in Fig. 4F), and we observed that subpopulations of pyramidal cells that were exposed to the cue exhibited sustained firing during the delay period in both control and SZ circuits (Fig. 4F). In the SZ circuit, sustained ectopic activity was often observed in the pyramidal neurons that did not receive the cue signal (Fig. 4, F and G). The model suggested that EPSCs from NMDARs via XL spines, but not AMPARs, are a critical factor for ectopic activity (Fig. 4H), which may interfere with the cue-evoked activity and be related to the impairment of working memory in SZ (*2*, *4*).

Overrepresentation of large spines in human postmortem SZ brains

We next examined the spine morphology of the human primary auditory cortex of 20 patients with SZ and 20 matched controls. Because spinophilin is a dendritic spine protein, and F-actin fills the spine, the fluorescence intensity of the F-actin blob that overlaps with the spinophilin puncta can be used to estimate the spine volume in immunohistochemical preparations (Fig. 5A and fig. S9) (*19*). The spine volume distribution of patients with SZ was significantly different from that of the matched controls ($P < 0.01$; Fig. 5B). Consistent with a previous report (*19*), we observed a loss of smaller spines in the SZ group (Fig. 5C). In the analysis of the mouse model, the definition of the XL spine was the functional boundary, where the amplitude of the intra-spine Ca^{2+} event increased steeply (Fig. 5D). Because functional experiments in human synapses are not possible, we compared spine volumes at thresholds of >0.8, >1.0, and >1.2 μm^3 and found that large spines were significantly increased in patients with SZ at all thresholds (Fig. 5C). For patients who had died by suicide, the statistical significance was more pronounced (Fig. 5D). We observed a significant correlation between F-actin and spinophilin in each individual spine (fig. S9E). This suggested that spine size was increased in the brains of SZ participants, excluding the alternative possibility that F-actin, but not spine volume, was somehow preferentially enhanced by disease. There is considerable evidence that the brains of patients with SZ exhibit subtle cytoarchitectural disorganization (*37*). Because of tissue fragility, SZ brains may undergo greater shrinkage following paraformaldehyde (PFA) fixation, which may have caused the large spines to appear more abundant in the SZ group. To test this possibility, we compared the thickness of brain sections before and after fixation and found no difference in the degree of shrinkage (fig. S9F). Therefore, we concluded that the overrepresentation of large spines exists in the brains of patients with SZ.

Optical prevention of XL spine generation restored working memory deficits

To determine the behavioral outcomes of XL spines, we returned to the animal model. The T-maze test revealed that both model mice showed impaired spatial working memory ($P < 0.05$ for *SETD1A* hKO mice, $P < 0.05$ for *DISC1* cKD mice; Fig. 6A and fig. S10A). Locomotor activity in the open-field and prepulse inhibition tests was not affected in the SZ model (fig. S10, B and C). To examine

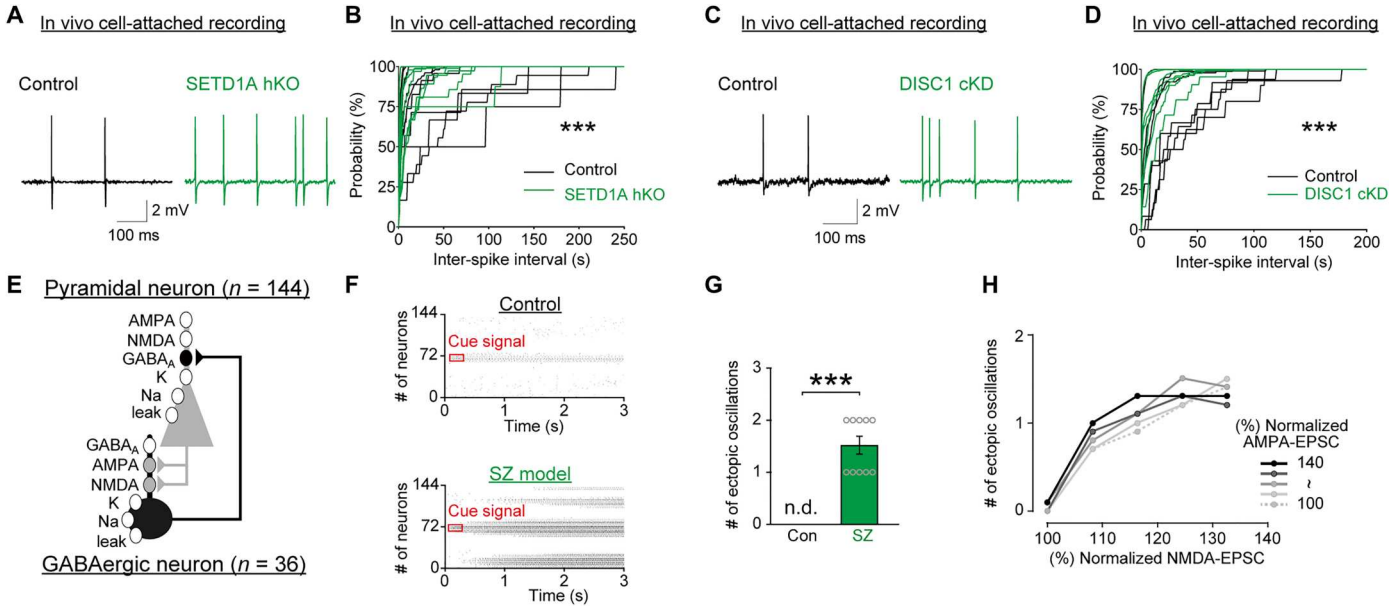

Fig. 4. Enhanced neuronal firing and unstable circuit dynamics in SZ models. (**A** and **B**) Representative traces of in vivo cell-attached recordings of the prelimbic and frontal association cortexes of *SETD1A* hKO mice at P60 to P75 (A). Cumulative probabilities of an individual recording (B). $n = 9$ to 10 cells per condition. (**C** and **D**) In vivo cell-attached recording of the prelimbic and frontal association cortexes of *DISC1* cKD mice at P60 to P75 (C). Cumulative probabilities of an individual recording (D). $n = 7$ cells per condition. (**E**) Leaky integration-and-firing network modeling of local circuits in the PFC. Parameters used for local circuit simulation are cited. (**F**) In silico raster plot of the model in (E). Following the application of a cue signal (depicted in red), cue-evoked oscillation was observed in control and SZ circuits. In the model in which raw data from SZ model neurons were applied, ectopic oscillatory activity was present. (**G**) Number of ectopic oscillations in each group ($n = 10$/each). (**H**) Ectopic oscillatory activity resulting from in silico manipulation of NMDAR and/or AMPA receptor (AMPAR) conductance. $n = 10$ simulations per condition. Experimental data derived from SZ neurons were AMPAR 138% and NMDAR 143%. ***$P < 0.001$. See also table S1 for measures and statics. Parameters used for local circuit simulation are available in table S3.

the relationship between XL spines and working memory performance, pyramidal neurons were visualized by intracellular injection of biocytin after T-maze testing. Working memory performance was negatively correlated with both the probability and cluster density of XL spines (probability, $r_s = -0.86$, $P < 0.01$; cluster density, $r_s = -0.84$, $P < 0.01$) (Fig. 6, B and C). Because neither working memory performance nor the increase in XL spines was observed at P50 (fig. S10, D to H), we hypothesized that the overrepresentation of XL spines contributes to working memory impairment. To test this hypothesis, we used our previously developed synaptic optoprobe, activated synapse (AS)–targeting photoactivatable Rac1 (AS-PaRac1), which can specifically label enlarged spines within 24 hours and induce selective shrinkage of AS-PaRac1–containing spines upon photoactivation (PA) (*28*, *38*). The number of AS-containing spines was comparable between *SETD1A* hKO and control mice (Fig. 6F); however, the size of AS-containing spines was significantly larger in hKO mice (Fig. 6, D and E), which prompted us to challenge the prevention of XL spine generation during late neurodevelopment using PA treatment with AS-PaRac1 (Fig. 6G). One day after the consecutive 9-day PA treatment of the bilateral PFC, the acute slices were prepared from the mice, and the pyramidal neurons were patch-clamped in the PFC to measure the membrane potentials and impedances, which were not affected by PA, suggesting that phototoxicity due to PA was negligible (fig. S10, J and K). The identical PA treatment in *SETD1A* hKO mice shifted the spine size distribution into a smaller population (Fig. 6H). The number of spines in the control mice was not affected by PA (Fig. 6I), which was presumably because of the compensation of active spine generation during development. The probability of XL spines was markedly reduced by PA, although the number of total spines was unaffected (Fig. 6H). Following the treatments of protocols #2 and #3, working memory performance assessed using the T-maze and Y-maze tests progressively deteriorated from P50 to P60 in the *SETD1A* hKO mice, whereas the treatment of protocol #1 prevented this progressive trajectory (Fig. 6J) without affecting locomotion activity (fig. S10H). The identical procedure did not affect working memory performance in the littermate controls (Fig. 6K). Together, we concluded that the prevention of XL spine generation during late neurodevelopment prevented the disease progression of *SETD1A* hKO mice.

DISCUSSION

Determining the causality between synaptic pathology and psychiatric disorders has been challenging because of the lack of functional studies of synapses in humans. Therefore, we focused on two disease-related genetic variations with large effect sizes: disruptive LoF mutations of the *SETD1A* and *DISC1* genes. Both mice models exhibited an overrepresentation of XL spines, which supralinearly boosted neuronal firing via NMDAR-dependent regenerative electrogenesis inside XL spines. Notably, the probability of XL spines was significantly increased in the postmortem brains of patients with SZ. Last, the probability of XL spines was negatively correlated with working memory in *SETD1A* hKO and *DISC1* cKO mice, and optical prevention of XL spine generation during development

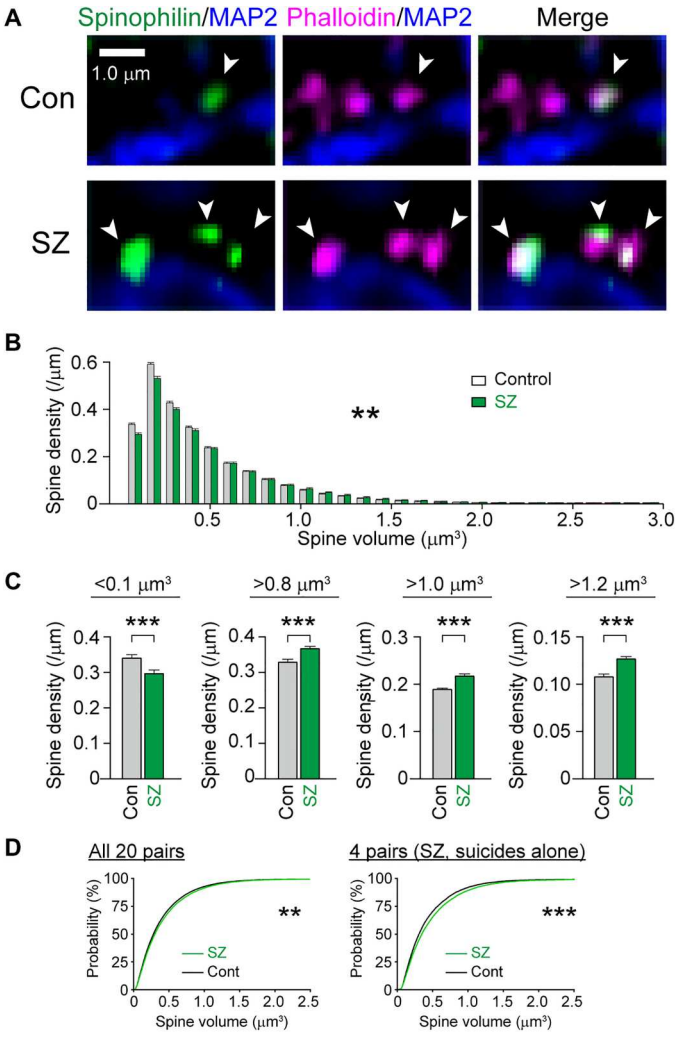

Fig. 5. Spine analysis of the SZ participants' postmortem brains. (**A**) Representative images of dendrites in the primary auditory cortexes of human of SZ participants and matched controls. Arrowheads: Protrusions identified as "spines" using deep learning. (**B**) Histograms of spine volumes in 20 SZ participants and 20 matched control participants. (**C**) Comparison of spine densities according to spine volume thresholds of >0.8, >1.0, and >1.2 μm^3. (**D**) Cumulative probability showing the significant increase of larger spines in SZ participants. Comparison between 20 SZ participants and matched controls (left), and between patients with SZ who died of suicide and matched controls (right). $^{**}P < 0.01$, $^{***}P < 0.001$. See also table S1 for measures and statics.

successfully rescued the deterioration of working memory in the SZ model (Fig. 7).

LoF variants of the *SETD1A* and *DISC1* genes are associated with both SZ and NDDs (*20*, *22*, *39*, *40*). Although SZ and NDDs share common genetic risk factors and clinical manifestations (*1*, *41*, *42*), the neural underpinnings of the substantial phenotypic overlap of these two disorders are poorly understood. The currently accepted hypothesis for SZ pathophysiology is neuronal hypoconnectivity due to the over-pruning of smaller spines (*43*), and loss of smaller spines was replicated in *SETD1A* hKO and *DISC1* cKO mice (Fig. 1, A and B). In addition, alterations in cortical γ-aminobutyric acid (GABA) neurons are involved in SZ pathophysiology (*44*). Regarding ASD, local hyperconnectivity and long-range hypoconnectivity have been proposed; moreover, an increase in spine density has been considered a possible contributing factor. Here, we propose that hyperconnectivity due to distorted neuronal computation via XL spines is one of the shared contributing factors to these disorders. Several clinical symptoms of SZ and NDDs are drug-resistant and extremely refractory. For example, hallucinations and delusions of patients with chronic SZ are often persistent. In patients with NDD, perseverative behaviors and repetitive cognition are also refractory. The extreme robustness of these persistent symptoms suggests the existence of a disorder-related neuronal ensemble that is easily activated. XL spines may be a contributing factor to these symptoms, and the high stability (*28*) and strong influence on AP generation of large spines are consistent with this hypothesis.

The ability for small numbers of spines to evoke an AP profoundly influences firing probability (P_n): $P_n = a_1 \times a_2 \times a_3 \times \ldots a_n$, where n represents the required number of synaptic inputs to evoke an AP (1 to 4 XL spines or ≥8 of the other spines), and a_n represents the probability for each spine to receive the synaptic input within a duration short enough for temporal summation. Because the relatively sparse activity is a functionally important feature of cortical layer II/III excitatory neurons (*45*), this multiplier equation intuitively suggests the unusual influence of XL spines on AP generation. The currently accepted dendritic computation for neuronal firing has three gating thresholds (*46*, *47*): (i) NMDA spike at the distal dendrite, (ii) Ca^{2+} spike through VDCCs at the proximal dendrite, and (iii) AP generation. Thus, neurons implement a hierarchical "synaptic democracy," in which incoming signals are filtered via integration to determine whether an AP is evoked. This is bypassed in neurons with XL spines, and evocation of the AP is potentiated by a small number of pathologically excitable "aristocratic" XL spines. Thus, the functional organization of the circuit, including highly regulated AP generation, is disrupted. A limitation of this study is that we are, at present, unable to provide direct evidence because no methods are presently available to specifically manipulate only XL spines. However, multiple findings support this notion. First, at P50, there was neither a significant increase in the probability of XL spines nor WM impairment in *SETD1A* hKO mice. By contrast, at P60, a significant increase in XL spines was detected, which significantly correlated with WM disturbance. In addition, the majority of AS-PaRac1–positive spines in P60 *SETD1A* hKO mice met the criterion of XL spines. Optical radiation for AS-PaRac1 from P50 to P60 markedly decreased the probability of XL spine development and completely blocked the progressive deterioration of WM performance in the *SETD1A* hKO mice. An identical manipulation did not affect WM performance in WT mice, suggesting that the elimination of non-XL spines did not affect WM performance. Together, it is feasible that optical elimination of the XL spines prevented progressive deterioration of WM performance in the *SETD1A* hKO model. Furthermore, our leaky integrate-and-fire model suggested that the overrepresentation of XL spines is prone to generating cue-irrelevant ectopic activity. The emergence of a disorder-related neuronal ensemble is consistent with the findings of a study using a different line of *SETD1A*$^{+/-}$ mice (*48*), which exhibited altered ensemble activity that was associated with pathological sensory cortical processing. Such distortion of neuronal ensembles is likely to compromise information flow within the brain, affecting cognitive and behavioral manifestations.

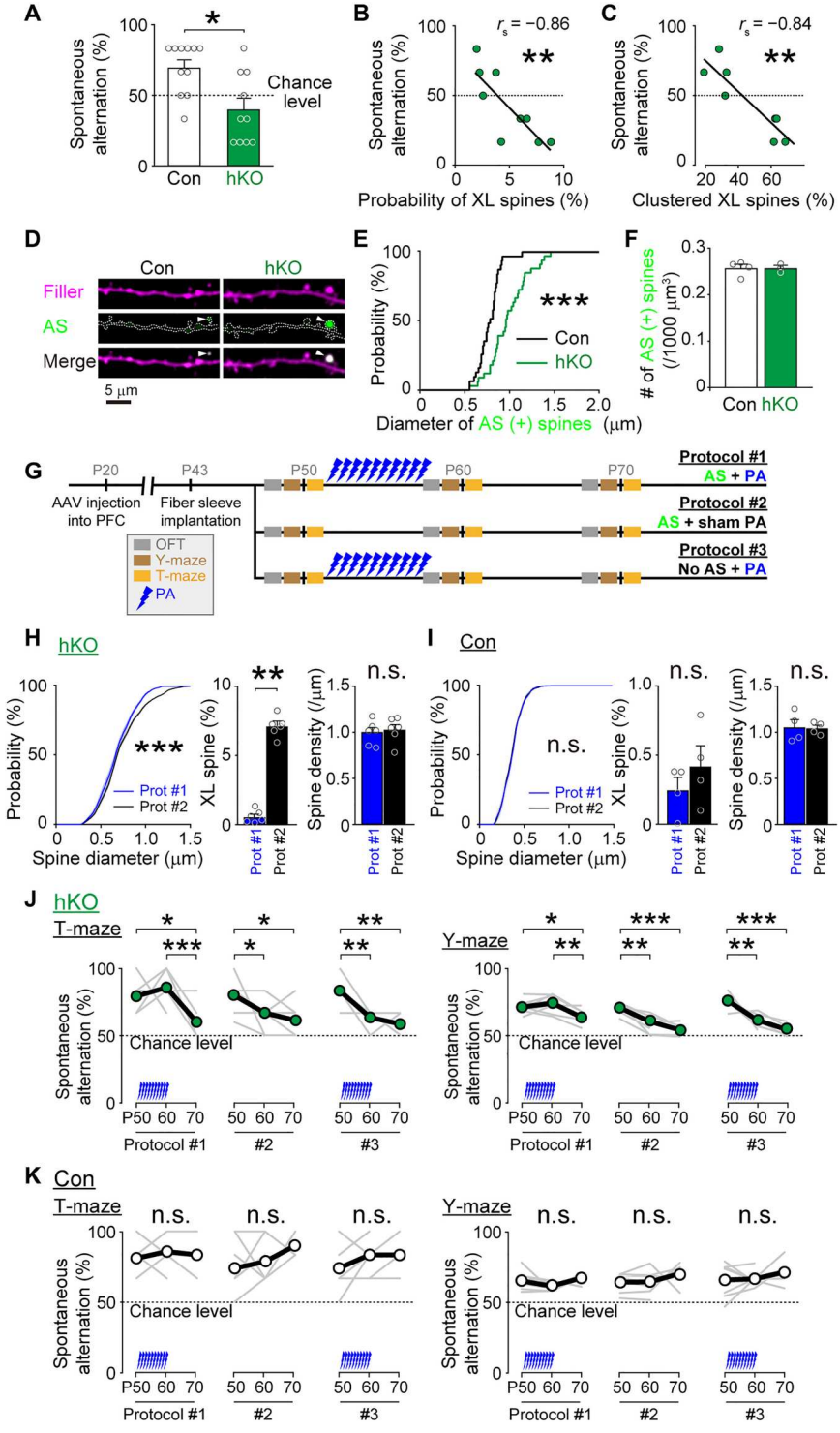

Fig. 6. Optical prevention of XL spine generation restored working memory deficits. (**A**) T-maze performance illustrating spontaneous alterations in *SETD1A* hKO mice. Circles indicate individual mice. (**B** and **C**) Probability of spontaneous alternations in the T-maze correlated with the prevalence (B) and cluster density (C) of XL spines in *SETD1A* hKO mice. (**D** and **F**) Representative images of AS-PaRac1–containing spines [(D), arrowheads] and comparisons of spine diameter (**E**) and number (F) of AS-PaRac1–containing spines between *SETD1A* hKO and control mice. (**G**) Experimental design. Mice were injected with adeno-associated virus (AAV) vectors in the bilateral PFC cortex at P20. After undergoing a sleeve implantation operation, mice were subjected to behavioral analysis and photoactivation (PA). (**H** and **I**) Comparisons of spine diameter, probability of XL spines, and spine density between *SETD1A* hKO (H) and littermate control mice (I) that received protocol #1 or #2. (**J** and **K**) Performance trajectory in the T-maze and Y-maze tests of *SETD1A* hKO (J) and littermate control mice (K) that received protocol #1, #2, or #3. **P* < 0.05, ***P* < 0.01, ****P* < 0.001. See also table S1 for measures and statics.

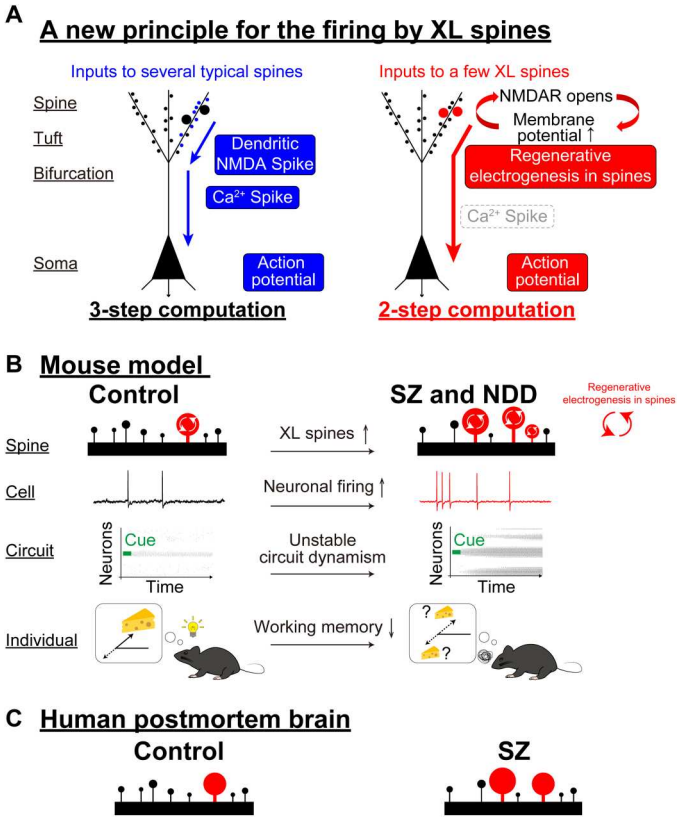

Fig. 7. Distorted neurocomputation by heavily weighted synapses in psychiatric disorders. (**A**) Activation of XL spines boosted neuronal firing via intra-spine supralinear voltage amplification, which is a previously unknown mechanism to control firing. (**B**) Overrepresentation of XL spines was correlated with the increase in firing, the generation of ectopic oscillation, and working memory impairment. (**C**) Overrepresentation of large spines in the auditory cortex of patients with SZ.

Although we demonstrated the trans-scale causality of XL spines in *SETD1A* and *DISC1* model mice, this did not account for the general principle of all populations of the disorders. Compared with the marked increase in XL spines in *SETD1A* and *DISC1* model mice, the group difference between the postmortem brains of 20 patients with SZ and 20 controls was modest. This may be because of species differences. However, given that the statistical significance was more pronounced in those who died of suicide, the heterogeneity of the disorders may have diluted the group difference. In mouse models, a significant increase in the number of large spines has also been observed in mice with NR1 KD (*49*) and calcineurin knockout (*50*), both of which are recognized as SZ models with working memory deficits (*51*, *52*). Maternal immune activation (*53*) and Cx3cr1 KO (*54*) mice, both of which are NDD animal models, exhibited significantly higher mEPSC amplitudes than their wild-type littermates, which is indicative of the overrepresentation of large spines in these models. Given the etiologic heterogeneity of these disorders, the regulatory molecular mechanisms for the pathological development of overabundant large spines are likely model-specific. However, the functional roles of large spine overabundance on distorted computation could be shared in these disorders. Thus, in certain subsets of diseases, distorted connectivity due to XL spines may be responsible, and stratification of patients based on functional connectivity patterns and genotypes may enable mechanism-oriented therapeutic strategies for each subtype.

MATERIALS AND METHODS

Ethical considerations

All animal experiments were approved by the Animal Care and Use Committee of RIKEN and the School of Medicine of Gunma University. All human experiments were approved by the Wako Third Research Ethics Committee of RIKEN and the Committee for Oversight of Research and Clinical Training Involving Decedents of the University of Pittsburgh. The experiments were conducted on the basis of the ARRIVE guidelines 2.0. The contents included in the ARRIVE Essential 10 checklist are described in table S1 or in the methods associated with each experiment.

Plasmid construction for DISC1 cKD

pCAG-ERT2-Cre-ERT2 was purchased from Addgene (no. 13777), and the ESARE promoter was a generous gift from H. Bito (University of Tokyo). Mutagenesis and subcloning of DISC1 (shRNA, short hairpin RNA), ERT2-Cre, mRFP (monomeric red fluorescent protein), tdTomato, and mVenus were conducted as previously described (*24*, *25*, *28*). Briefly, microRNA (miRNA)-based shRNA against DISC1 was generated by annealing the top (TCG AGA AGG TAT ATT GCT GTT GAC AGT GAG CGA GGC AAA CAC TGT GAA GTG CTA GTG AAG CCA CAG ATG TAG CAC TTC ACA GTG TTT GCC GTG CCT ACT GCC TCG C) and bottom (TCG AGC GAG GCA GTA GGC ACG GCA AAC ACT GTG AAG TGC TAC ATC TGT GGC TTC ACT AGC ACT TCA CAG TGT TTG CCT CGC TCA CTG TCA ACA GCA ATA TAC CTT C) strand oligos for miR30 (DISC1 shRNA is underlined), which was inserted at the XhoI site of intron 1 of human hemoglobin (NM_000518) to generate an miR30 shRNA minicassette. The minicassette was subcloned immediately downstream of tdTomato in the pAAV-EF1a-DIO-tdTomato-WPRE vector. Scrambled shRNA, GCC CGA AGC GTT AAA AGG T, was used as the negative control. Depending on the experiments, the proper promoter, DIO, Cre, and fluorescence proteins were subcloned. Plasmid amplification was performed using JM109 competent cells.

Animals

SETD1A$^{(+/-)}$ knockout mice in a C57BL/6 N background were obtained from M. Kano (*23*). *DISC1* LoF mice in a C57BL/6J background were a gift from K. Kaibuchi (*30*). The generation of DISC1 KD mice was genetically transferred with DISC1 shRNA (*24*) constructs using adeno-associated virus (AAV) vectors into C57BL/6J (see the "Virus injection" section below).

AAV production

According to a previously published protocol (*28*), we packaged the AAV helper-free system (Agilent Technologies, Santa Clara, CA), the pRep-Cap (AAV5; Applied Viromics, Fremont, CA), and the pHelper plasmid. AAV was purified using a cesium chloride density gradient, combined with ultracentrifugation. Virus titer was determined using quantitative real-time polymerase chain reaction analysis (SYBR green; Takara Bio Inc., Shiga, Japan).

Virus injection

Mice at P18 to P20 were anesthetized with isoflurane. d-Mannitol (4 μg/g of body weight) and dexamethasone (7 μg/g of body weight) were also administered intraperitoneally to prevent brain swelling. Subcutaneous injections of ketoprofen (40 μg/g of body weight) and penicillin/streptomycin (4 U/g of body weight) were administered for four consecutive days from 1 day before the operation to prevent inflammation. The skull was exposed over the frontal association cortex according to stereotactic coordinates. A stainless steel drill (ϕ 0.5 mm; 19007-05, Fine Science Tools, Foster City, CA) was used to generate a small burr hole (ϕ < 1 mm) in the skull, and 0.5 μl of AAV (SETD1A hKO: AS-Venus 1.65×10^{13}, DIO-tdTomato 1.46×10^{12}, mixed with CaMK2-Cre $1.5 \times 10^{8-10}$, DISC1 cKD: sDIO-mRFP-Disc1 shRNA or scrambled shRNA 1.8×10^{13} to 2.5×10^{13} genome copies/ml, mixed with ESARE-sCre $6.0 \times 10^{9-12}$ genome copies/ml) was injected using a glass pipette (tip diameter, 40 to 45 μm; beveled at 45°) at a rate of 80 nl/min using a syringe pump (Legato130; KD Scientific, Holliston, MA). The location of the injection site was standardized among animals using stereotaxic coordinates (anterior-posterior = +1.8 mm; medial-lateral = +0.6 mm; dorsal-ventral = +0.4 mm) of the skull. The pipette was retracted 5 min later, the scalp was sutured, and antibiotic ointment (Hibix ointment; Fujita Pharmaceuticals, Tokyo, Japan) was applied to the wound.

Validation of DISC1 cKD

Western blotting and immunocytochemistry were performed to examine the DISC1 cKD mice. Two days after the 293FT cells were transfected (Lipofectamine LTX; Thermo Fisher Scientific, Waltham, MA) with pCAG-DIO-tdTomato-DISC1 shRNA, pCAG-DISC1-HA, and pCAG-Cre (2:0.5:0.5 μg per well of six-well plate), cells were lysed in radioimmunoprecipitation assay buffer [150 mM NaCl, 50 mM tris-HCl (pH 7.4), 1% NP-40 (v/v), 0.5% sodium deoxycholate (v/v), 0.1% sodium dodecyl sulfate (v/v), 1 mM dithiothreitol, and protease inhibitor cocktail (cOmplete; Roche Diagnostics, Indianapolis, IN)] via sonication on ice, and cell debris was cleared by centrifugation. Protein concentration was measured using a BCA Protein Assay Kit (Thermo Fisher Scientific). Ten micrograms of protein per lane was run on an SDS–polyacrylamide gel electrophoresis gel, transferred to a membrane, and immunoblotted with anti-hemagglutinin (HA) (M180-3; Medical & Biological Laboratories Co., Ltd., Aichi, Japan) and anti–β-actin (sc-47778; Santa Cruz Biotechnology Inc., Dallas, TX) antibodies. The HA immunoreactivity (IR) of each band (the net signal after subtracting the background signal, which was obtained from the region adjacent to the band) was measured using the Fiji software (NIH, Bethesda, MD). For the validation of cKD in vivo, C57BL/6J mice that were transduced with KD constructs were euthanized and sacrificed by transcardiac perfusion with 4% PFA on P20. Their brains were postfixed overnight in the same fixative at 4°C and treated as described below (see the "Immunohistochemistry and histological analyses" section).

Immunohistochemistry and histological analyses

Brains were coronally sectioned (150 to 300 μm) using a vibratome (VT1200S; Leica, Wezlar, Germany) at an angle of 20°, so that the primary trunk of the apical dendrite was parallel to the section angle, which ensured that the majority of the dendrite trees and soma remained intact. Sections were permeabilized with 2.5% normal goat serum (v/v) in phosphate-buffered saline (PBS) with 0.3% Triton X-100 (v/v) for 1 hour at room temperature, before incubating overnight at 4°C with primary antibodies. After rinsing with PBS (five times for 8 min each), the sections were stained with the corresponding secondary antibodies before mounting.

EM analysis

Scanning electron microscopy (SEM) of XL spines in mouse PFC was performed by focused ion beam (FIB)–SEM as described previously (*55*). Briefly, two pairs of control and conditional DISC1 KD mice were anesthetized with pentobarbital and perfused with modified Karnovsky fixative [0.8% PFA (PFA: TAAB Laboratories Equipment Ltd., UK) and 1.5% glutaraldehyde (Nacalai, Japan) in 0.15 M sodium cacodylate buffer containing 2 mM $CaCl_2$ (pH 7.4)]. The brains were postfixed with 4% PFA overnight and coronally sectioned into slices of 100-μm thickness with a vibratome (DSK Pro7). The slices were serially fixed with reduced OsO_4 (2% OsO_4 and 1.5% potassium ferrocyanide) and OsO_4 (2%), and then metal-stained with uranyl acetate and lead aspartate. For embedding into resin, the slices were dehydrated with a graded series of ethanol solutions, immersed in propylene oxide twice, and gradually equilibrated with Durcupan resin (Sigma-Aldrich). The slices containing the PFC were flat-embedded and polymerized first, re-embedded into a columnar shape resin block, and then the area of interest was exposed to the surface with a diamond knife. After coating with a thick carbon layer over the block, serial images (~350) of layer I/II of the dorsomedial part of the PFC were collected with a scanning electron microscope (Scios, FEI) equipped with a FIB and at a 40-nm Z-step at an acceleration voltage of 1.5 kV. Images were captured at a magnification of ×17500 and with 6144 and 4096 pixels for the *x* and *y* axes, respectively. After a correction of *y*-axis distortion due to a tilt observation by increasing the number of pixels for the *y* axis to 5198, the size of a pixel for *x*, *y*, and *z* is 1.927, 1.927, and 40 nm, respectively. All images were analyzed and visualized with TrakEM2 in Fiji (*56*). Within each image volume (approximately 12 by 10 by 15 μm), dendritic spines were searched and manually segmented, and the volume of the spine, the area of PSD, and the cross-sectional area of the spine check were measured at the largest 30 spines.

Confocal imaging

Confocal imaging was performed using an inverted microscope (IX81; Olympus, Tokyo, Japan) and an oil-immersion objective lens [UPlanSApo, 60×, 1.35 numerical aperture (NA)]. The excitation wavelength was 473 nm for imaging mVenus and Alexa Fluor 488 and 559 nm for mRFP. Images were acquired at 1 to 2× digital zoom, 1024 × 1024 pixels, 4 ms/pixel dwelling time, and a *z*-axis step size of 0.37 μm.

Acute slice preparation

Mice at P60 to P180 were deeply anesthetized and transcardially perfused with ice-cold *N*-methyl-D-glucamine (NMDG) solution (92 mM NMDG, 2.5 mM KCl, 1.25 mM NaH_2PO_4, 30 mM $NaHCO_3$, 20 mM HEPES, 25 mM glucose, 2 mM thiourea, 5 mM ascorbic acid, 3 mM Na-pyruvate, 0.5 mM $CaCl_2$, and 10 mM $MgCl_2$), as described previously. Brains were coronally cut at a 30° angle into 250-μm sections on a vibratome using Merkur blades. The slices were transferred immediately to NMDG solution for 10 min at 35°C and incubated in HEPES holding solution (92 mM NaCl, 2.5 mM KCl, 1.25 mM NaH_2PO_4, 30 mM $NaHCO_3$,

20 mM Hepes, 25 mM glucose, 2 mM thiourea, 5 mM ascorbic acid, 3 mM Na-pyruvate, 2 mM $CaCl_2$, and 2 mM $MgCl_2$) for 1 hour at room temperature before transferring to a recording chamber (TC-324B; Warner Instruments, Hamden, CT) containing artificial cerebrospinal fluid (ACSF) (125 mM NaCl, 2.5 mM KCl, 1.25 mM NaH_2PO_4, 26 mM $NaHCO_3$, 25 mM glucose, 2 mM $CaCl_2$, and 1 mM $MgCl_2$) at 33° to 35°C for two-photon imaging and whole-cell recording.

Whole-cell recording

Whole-cell patch-clamp recording was performed using a MultiClamp 700B (Molecular Devices, San Jose, CA). Micropipettes (BF150-86-10; Sutter Instrument, Novato, CA) were pulled with a P1000 (Sutter Instrument) and fire-polished using a microforge (MF-900; Narishige, Tokyo, Japan). For the voltage-clamp recordings, the pipette resistance was 4 to 5 megohms. For the current-clamp recordings, the pipette resistances for the firing pattern/back-propagation and line-scan experiments were 5 to 7 megohms and 8 to 10 megohms, respectively. The intracellular solution for the voltage clamp was a Cs-based internal solution[51][130 mM Cs-gluconate, 10 mM CsCl, 10 mM Hepes, 0.1 mM EGTA, 10 mM Na_2-phosphocreatine, 4 mM Mg–adenosine 5′-triphosphate (ATP), 0.3 mM Na_2–guanosine 5′-triphosphate (GTP), and 0.05 mM Alexa Fluor 488 (pH 7.25)]. The K-based internal solution was used for the current clamp [130 mM K-gluconate, 10 mM KCl, 10 mM Hepes, 0.1 mM EGTA, 10 mM Na_2-phosphocreatine, 4 mM Mg-ATP, 0.3 mM Na_2-GTP, and 0.05 mM Alexa Fluor 488 (pH 7.25)]. Ca^{2+} imaging during current-clamping was performed in the K-based internal solution [130 mM K-gluconate, 10 mM KCl, 10 mM HEPES, 10 mM Na_2-phosphocreatine, 4 mM Mg-ATP, 0.3 mM Na_2-GTP, 0.05 mM Alexa Fluor 594, and 0.1 mM Cal-520 (pH 7.25); AAT Bioquest, Sunnyvale, CA]. The liquid junction potential was −10 mV and corrected. The bridge balance and pipette capacitance neutralization were checked during the current-clamp mode. Data were filtered at 2 kHz and digitized at 20 kHz for the voltage clamp and filtered at 10 kHz and digitized at 20 kHz for the current clamp. All data were acquired using AxoGraph X (AxoGraph, Sydney, Australia) with the interface of NI USB-6363 (National Instruments, Austin, TX). All analyses were performed using AxoGraph X and Igor Pro 8.03 (WaveMetrics Inc., Lake Oswego, OR). The AP voltage threshold was defined by the voltage when the first time derivative exceeded 20 V/s. The voltage threshold was defined as the EPSP amplitude when an AP was fired.

In vivo cell-attached recordings

Mice were anesthetized with 2% isoflurane and a single injection of urethane (1.5 g/kg of body weight, ip) alongside atropine sulfate (0.2 mg/kg of body weight, ip) to suppress mucus secretion. A hemisphere trapezoidal craniotomy covering the prefrontal and somatosensory regions was performed. A customized metal head plate with a recording chamber (Saijo Inx Co., Ltd., Kyoto, Japan) was mounted on the skull contralateral to the recording site using dental cement (Shofu Inc., Kyoto, Japan) to tightly secure the head in the stereotaxic apparatus (Narishige, Tokyo, Japan). The recording chamber was filled with HEPES-buffered ACSF, and a durotomy was carefully performed using a fine handmade hook. ACSF was gently perfused through the recording chamber to control bleeding, after which low-melting agar dissolved in HEPES-buffered ACSF was applied to the brain surface. A rectangular coverslip (<0.1-mm thickness; Matsunami Glass, Kishiwada, Japan) that covered approximately half of the exposed brain surface was applied. Mice were closely monitored for breathing (MP100 pulse transducer; AD Instruments, Dunedin, New Zealand) and warmed to 37°C using a heating pad (TR-200; FST, Foster City, CA). The pipettes were filled with the K-based internal solution containing 50 μM Alexa Fluor 488. Positive pressure (25 kPa) was applied as the pipette went through the pia matter and was subsequently reduced to 6 to 8 kPa. When the pipette tip was adjacent to the soma membrane of the target cell (tdTomato-positive), positive pressure was released, followed by slight negative pressure to optimize the seal. Cell-attached recordings (20- to 50-megohm seal resistance) were performed for 15 min (5 min × 3 sessions), and cells that exhibited constant firing during all three sessions were analyzed. The reference electrode was placed in the ACSF-containing space of the headgear.

Two-photon imaging and glutamate uncaging

Two-photon imaging was performed using an upright microscope (BX61WI; Olympus) equipped with an FV1000 laser scanning microscope system (W2, FV1000; Olympus) and water-immersion objective lenses (XLPLN25XWMP2, 25×, 1.05 NA). For the quality control of the microscope setting, including laser alignment, we used calibration microbeads (catalog no. 18859, 0.5-μm diameter beads; catalog no. 18860, 1-μm diameter beads; Polysciences Inc. Warrington, PA). A mode-locked, femtosecond-pulse Ti:sapphire laser (MaiTai DeepSee; Spectra-Physics, Mountain View, CA) was used at 940 nm for cell-attached recording (tdTomato and Alexa Fluor 488), 980 nm for mRFP or Cal-520 imaging, and 1000 nm for dual-color imaging of mRFP and Alexa Fluor 488. For two-photon uncaging, another Ti:sapphire laser (MaiTai HP) was used at 720 nm. For in vitro imaging, 10 to 40 images (10 to 14× digital zoom; 1024 × 1024 pixels) were captured with a *z*-axis step size of 0.5 or 1.0 μm. Two-photon Ca^{2+} imaging was performed at 15 Hz for 5 s. Line-scan imaging through spines and dendrites was performed at 700 to 800 Hz for 6 to 7 s. For glutamate uncaging (*26*), a glass pipette (70- to 120-μm tip diameter of GC150TF-10; Harvard Apparatus) filled with 10 mM MNI-glutamate (Tocris Bioscience, Bristol, UK), dissolved in ACSF containing 100 μM picrotoxin (Tocris Bioscience), was applied locally at 20 μl/min to dendrites via an injector (Legato100; KD Scientific, Holliston, MA). The uncaging of MNI-glutamate at spine heads was performed at 720 nm with a pulse duration of 0.72 ms. Because the summation of synaptic inputs over a dendritic branch is counterbalanced by inhibitory inputs, the experiment was also performed in the absence of picrotoxin. Therefore, for the strict quantification of excitatory synaptic integration, all subsequent experiments were performed in the presence of picrotoxin to exclude the influence of GABA. To mimic physiological synaptic inputs, the two-photon laser power was adjusted such that the ranges of uncaging-evoked EPSP amplitudes and kinetics were identical to those of mEPSP (fig. S5, A and B). Because voltage-dependent Na^+ channels open near the AP threshold, cation entry via this channel could affect the measured EPSP value, which could result in misinterpretation of synaptic summation. To avoid this confounder, we compared EPSP values upon synchronous synaptic inputs in the presence or absence of tetrodotoxin (TTX) (1 μM), which is an inhibitor of this channel. The AP threshold in the absence of TTX and the maximum amplitude of the somatic EPSP in the presence of

TTX were not significantly different (fig. S5, H to L). This supported the use of the AP threshold as a proxy for the maximum amplitude of the somatic EPSP when the neuron fired.

In vivo spine manipulation by optogenetics

In vivo two-photon imaging of the Fr2 area was performed from the pia to a depth of 150 μm, and the number of AS-PaRac1-Venus was calculated, among which puncta within 2-μm diameter were approximated as AS-containing spines. Gray matter volume was calculated from the imaged area, excluding the vascular lumen, and the number of AS-PaRac1-Venus puncta per 1000 μm^3 was determined. Fiber sleeves (ADAL1, 2.5 mm outer diameter, Thorlabs, Newton, NJ) were placed onto the exposed skull, immediately above the bilateral frontal cortex (AP = +2.5; ML = ±1.0). Before PA, the optical fibers (BFYF4LF01; core diameter of 400 μm, 0.39 N.A.; Thorlabs) were connected to the mice via the fiber sleeves and removed after PA. Photostimulation was carried out using the COME-2 series (Lucir, Japan), which consisted of 457-nm laser diodes and an optical swivel. The laser diode was measured through the skull and adjusted to an output of 20 mW, immediately after passing through the skull. The light pulse was delivered for 150 ms at 1 Hz for 1 hour, and the process was controlled by customized LabView programs (National Instruments, Austin, TX).

Measurement of Ca^{2+} transients

The membrane potential was set at −70 mV using a subtle current injection, and the intensity of the uncaging laser was adjusted to evoke an EPSP in typical-sized spines at an amplitude of 0.9 to 1.5 mV [similar to mEPSPs in terms of the amplitude and kinetics (fig. S3, A and B)]. Because cortical pyramidal neurons are sensitive to sequential synaptic activation (*32*), synaptic activation was ordered from the distal to proximal branches. TTX was not included in the perfusion buffer to enable AP firing, which only occurred with uncaging. Upon glutamate uncaging at three to five XL spines, the spine with a z-center point that was nearest to the *z* plane of the parental dendrite was selected for imaging. Depending on the experiment, TTX (1 μM; FUJIFILM, Japan), Cd^{2+} (300 μM; FUJIFILM), or D-AP5 (250 μM; Alomone Labs, Jerusalem, Israel) was added.

AMPA- and NMDA-EPSC measurements

Neurons in the voltage-clamp mode were subjected to glutamate uncaging in the presence of TTX (0.5 μM) and picrotoxin (100 μM). Laser power was adjusted to 12 mW and the two-photon pulse duration was 0.72 ms. The membrane potential was maintained at −80 mV (after correction for the liquid junction potential) for the AMPA-EPSC measurement, and NMDA-EPSCs were measured at a holding potential of +40 mV with the AMPAR antagonist 6-cyano-7-nitroquinoxaline-2,3-dione (50 μM; Alomone Labs).

Image quantification

Images in the *x*-*y* plane were stacked by the summation of fluorescence values at each pixel. For each channel, the background intensity was subtracted from the fluorescence intensity of each spine.

Sholl analysis

Concentric circles at 20-μm increments were centered on the neuronal soma, and the number of dendritic intersections at each circle was counted alongside the numbers of dendritic branch points and dendritic terminals within each circle.

Spine head measurements

NeuronStudio method

Z-stacked dendritic images were subjected to automatic tracing and reconstruction using the NeuronStudio software (Icahn School of Medicine at Mount Sinai). The name of the stacked images was anonymized to ensure that the analyzers were blinded to group allocation after the completion of the statistical analyses.

Gaussian function fitting method

The electrophysiological recordings were performed by K.O.-N., and the acquired images were quantified in a blinded manner by N.S. After the background signals were subtracted from the images, the axial profile of the fluorescence intensity of the Z-stacked spine images was fitted to a Gaussian function using Microsoft Excel Solver. To measure the spine head diameter, the full width at half maximum of each fluorescence peak was obtained from the axial profile of the best Gaussian fit.

Clustering assessment of XL spines

Fifteen simulated model cells were built and statistically compared with data from the experimentally observed neurons. First, the distance to the nearest neighbor for each XL spine was measured using the information of the neuron reconstructions in the NeuronStudio software. Model cells with a random spine size distribution but identical topological information were constructed by swapping the spine sizes of all spines by random permutation. A two-sample Kolmogorov-Smirnov test was used to compare the experimentally observed distribution and the probability distribution of the model cells.

Behavioral analysis

Mice were housed under standard laboratory conditions (12-hour light/dark cycle with food and water available ad libitum). All behavioral analyses were performed in a dimly lit room (100 lux) during the light phase. The experimenter was blinded to group allocation for all behavioral experiments. Tests were conducted on separate days in the following order: 1-day handling, open-field test, and prepulse inhibition.

Handling

Before the behavioral analyses, mice were acclimatized to the environment and handled by the experimenter. After gentle manual handling of the mouse for 10 min, the mouse was immediately subjected to the open-field test.

Open-field test

Mice were placed in and allowed to explore a square open-field arena (50 × 50 cm) with 50-cm high walls for 10 min. Locomotor activity and the spent time in each zone were automatically evaluated by a video tracking system (TimeOF1, O′Hara & Co., Japan).

Prepulse inhibition assay

Prepulse inhibition was calculated using a commercially available startle chamber (SR-LAB; San Diego Instruments, San Diego, CA). Each trial consisted of a 20-ms pre-pulse period, a 100-ms delay period, and a 40-ms startle pulse period. Under a controlled 70-dB background white noise, 50 trials were presented in a pseudo-random order with 10 background-alone trials, 10 startle-alone (120 dB) trials, and 30 prepulse (74, 78, and 86 dB) and startle

trials. The average across each of the 10 trials was used to calculate the percentage of prepulse inhibition.

T-maze test

The T-maze consisted of a gray plastic start arm (38-cm length, 10-cm width, and 25-cm height) and two goal arms (30-cm length, 9-cm width, and 25-cm height). The mice were placed in the start arm and forced to visit one goal arm by blocking access to the other arm. The mice were then returned to the start arm for the choice run, in which both goal arms were open. Spontaneous alternation was scored when the mouse selected a different goal arm from that selected during the forced run.

Y-maze test

The apparatus was made of gray plastic and comprised three compartments [3.6 cm (*W*) bottom and 12.5 cm (*W*) top, 37.5 cm (*L*), and 12 cm (H)] radiating out from the center platform (3.6 × 3.6 × 3.6 cm triangle). Each mouse was placed in the center of the maze and allowed to explore freely for 12 min.

Visualization of dendritic morphology

Acute slices of the PFC were prepared, and whole-cell patch-clamp recordings were performed from layer II/III pyramidal cells to visualize dendrite and spine morphology. Potassium-based internal solution supplemented with 0.4% biocytin (B4261, Sigma-Aldrich) was used. ShRNA-infected (i.e., red fluorescent) pyramidal cells in DISC1 cKD mice were identified under an epifluorescence microscope (BX61WI; Olympus). After recordings, slices containing biocytin-filled neurons were fixed overnight with 4% PFA. Fixed slices were permeabilized with 2.5% normal goat serum (v/v) in PBS with 0.3% Triton X-100 (v/v) for 1 hour at room temperature and subsequently incubated overnight with streptavidin–Alexa Fluor 488 (1:1000; S32354, Invitrogen) in PBS with 2.5% normal goat serum (v/v) and 0.3% Triton X-100 (v/v). Confocal microscopy was performed as described above. The apical tuft dendrites of layers II/III pyramidal cells in the prelimbic and frontal association cortices were imaged in a blinded manner. Spine head quantification was performed using the NeuronStudio software as described above.

Spine morphology of postmortem brains

Tissue processing and image collection

At University of Pittsburgh brain bank, the primary auditory cortex was dissected from 20 participants diagnosed with SZ and 20 control participants, who were matched for sex and as closely as possible for age, postmortem interval, and handedness (*19*). Detailed immunohistochemical procedures are described elsewhere (*19*). Briefly, to visualize the dendritic spines, we used two markers in combination: a polyclonal antibody against spinophilin (AB5669; Millipore, Billerica, MA), a protein that is specific to spine heads, and Alexa Fluor 568 phalloidin (A12380; Invitrogen) for detection of F-actin, which is also highly enriched in dendritic spines.

Image processing and analysis

Image acquisition was performed at University of Pittsburgh, for which resultant data have been published previously (*19*). An identical image dataset was shared and analyzed at RIKEN. First, three-dimensional (3D) stacked images were deconvolved using the AutoQuant adaptive blind deconvolution algorithm (AutoQuant X3, version 3.1; MediaCybernetics, Rockville, MD), and the resultant images were automatically analyzed using MATLAB R2021a (MathWorks, Natick, MA) in the manner described below. All voxels in each stacked image were normalized from 0 to 1, and adaptive thresholding was executed to binarize both phalloidin and spinophilin channels. The binarized phalloidin channel and spinophilin channel were merged to obtain overlapping images. Phalloidin blobs with a spinophilin blob overlap of >2% were extracted as "spine candidate blobs," and their statistical properties were measured. Blobs with an area >10 μm^3, <0.029 μm^3, or a spinophilin area greater than the phalloidin area were excluded from subsequent analyses.

Spine classification using deep learning

Microsoft Lobe, an image recognition platform based on a pretrained deep convolutional neural network (ResNet-50 V2), was used to create and train the spine classification models. For supervised learning, 5758 images were manually labeled as "Spine," whereas 5761 images were labeled as "Non-spine." These labels were independently determined by two experts (K.O.-N. and N.S.), and only those images with which both experts agreed were used as supervisory images. We created multiple models, which were trained using different supervisory images, and model performance was evaluated using the receiver operating characteristic (ROC) curve (fig. S9C). We implemented the best model using the TensorFlow package (version 2.5.0), which provides a Python application programming interface (version 3.8.10) for tensor manipulation. The structures that exhibited probability values higher than the cutoff value were classified as Spine. The optimal cutoff values for spine probability were determined by the ROC curve mentioned above.

Reconstruction of spines on the dendrite

From the 3D stacked images with well-preserved MAP2-IR staining, we reconstructed 3136 dendrites greater than 30 μm in length using Neurolucida (MBF Bioscience, Williston, VT). MAP2-IR is significantly decreased in SZ (*52*, *53*) and so is inappropriate for dendrite thickness quantification, but the center coordinates of the dendritic shaft can be accurately tracked. The coordinates that depict dendritic morphology in the Neurolucida platform were converted into MATLAB coordinates, in which the information of the deep learning certified spines was integrated, resulting in the 3D reconstruction map with precise coordinate information of the spines and dendrites. Spines with a distance of 6 μm or less between the center coordinates of a dendrite shaft and spines were considered the spines that emerged from the dendrite. Spine density calculated using this method is consistent with previously reported human spine densities (*54*). The cluster analysis of spines was performed according to the coordinates. Data analysts were blinded to diagnoses until the data analyses and subsequent statistical procedures had been completed.

Modeling of pyramidal neurons

Simulations of AP generation were performed using the NEURON 7.7 simulation platform (*27*) for an extended multicompartment model of a reconstructed layer II/III pyramidal neuron from the prelimbic cortex. One to 11 spines in eight distal tufts of the dendrite were incorporated into the model cell; the remaining dendrites did not have spines, such that only the incorporated spines received synaptic inputs. The majority of the known intrinsic and synaptic ionic currents were included in the model (*54*), and appropriate kinetics were obtained from mouse neocortical pyramidal neurons. The model with spines had a membrane potential of −73 mV. The passive electrical properties of the model consisted of axial

resistivity, membrane resistivity, and membrane capacitance of 100 ohm·cm, 80,000 ohm·cm^2, and 1.2 μF/cm^2, respectively. Spines were 1 μm apart and modeled as cylindrical compartments with a spine neck length of 0.5 μm and diameter of 0.2 μm and a spherical head with a diameter of 0.5 to 1.0 μm. The spine model comprised a membrane capacitance of 1.2 μF/cm^2 and a neck resistance of 500 megohms. Table S2 provides all the model parameters of each segment. Parameters were optimized until they achieved good agreement with the experimental data, and the number of spines, spine volume, and channel conductance required to generate an AP were investigated. Simulations closely followed the experimental protocol. To mimic the glutamate uncaging experiments, each spine was activated individually. Spines were then coactivated in increasing numbers, with an interval of 0.72 ms between activations, and the change in the membrane potential was monitored at the stimulated spine, tuft dendrite, trunk of the dendrite, and cell body. Quantification was identical to that used in the wet experiments. To mimic the VDCC blocking experiments, calcium-activated potassium channel conductance, and VDCC conductance were eliminated. The peaks of AMPAR and NMDAR conductance were based on experimental observations. Each conductance was assigned according to the spine head diameter. To mimic the synchronous activation of spines, the typical-sized spine diameter was set to 0.5 μm, whereas the diameter of XL spines was set to 1.0 μm. First, the glutamate conductance for the typical-sized spine was determined to ensure that a single-spine–evoked EPSP was 0.9 to 1.5 mV at the soma, consistent with the wet experiments. The glutamate conductance for XL spines was then calculated according to the correlation between the spine diameter and glutamate conductance (Fig. 3, J and K). Consequently, the conductance for AMPARs and NMDARs at the spines fell in the ranges of 0.9 to 20.3 nS and 2.7 to 17.5 nS, respectively. AMPA-EPSCs were modeled as double exponentials with a rise time of 1 ms, a decay time of 9 ms, and a reversal potential of 0 mV. NMDA-EPSCs were also modeled as double exponentials with a rise time of 10 ms, a decay time of 50 ms, and a reversal potential of 0 mV. The kinetics of the NMDA-EPSC were modeled using the following function:

$$g(V) = g\max(e^{-t/50} - e^{-\frac{t}{10}})/(1 + 0.3e^{-0.08v})$$

where V is the membrane potential (in millivolt).

PFC circuit model

The procedure was performed according to the previously published protocol (*36*). Briefly, the neurons (pyramidal cells and interneurons) were single compartments, and the leaky integrate-and-fire model included NMDAR, AMPAR, $GABA_A$ receptor, persistent Na^+, calcium-dependent potassium, and leak channels. Subtle parameter modifications were performed with respect to βk, pyramidal-pyramidal connective weight, pyramidal-interneuron connective weight and interneuron-pyramidal connective weight (table S3).

Materials design analysis reporting and statistical analysis

Sample size determination

No statistical methods were used to predetermine sample sizes. Sample sizes were chosen to be similar to those reported in previous works.

Randomization

Animals and samples were assigned randomly to control and experimental groups.

Blinding

Investigators were blind to the group allocation during all behavioral experiments. Analyzers were blind to the group allocation for spine head measurements.

Inclusion/exclusion criteria

Mice were excluded if the virus expression was not satisfactory. Mice that did not enter all arms (2 in 22 mice) in the Y-maze test were excluded from further analysis. In electrophysiological recordings, neurons that failed to complete a series of recordings were excluded from further analysis, and recordings with excessive noise contamination or unstable baseline were abandoned. Most of the exclusion criteria were established a priori, but for problems noticed during the experiment, the exclusion criteria were based on literature references to similar experiments. Statistical analyses were performed using the R software (The R Foundation, Vienna, Austria). All data are presented as means ± standard error of the mean. Detailed statistical information is provided in table S1.

Supplementary Materials

This PDF file includes:

Figs. S1 to S10
Tables S1 to S3

REFERENCES AND NOTES

1. N. de Lacy, B. H. King, Revisiting the relationship between autism and schizophrenia: Toward an integrated neurobiology. *Annu. Rev. Clin. Psychol.* **9**, 555–587 (2013).
2. A. Meyer-Lindenberg, J. B. Poline, P. D. Kohn, J. L. Holt, M. F. Egan, D. R. Weinberger, K. F. Berman, Evidence for abnormal cortical functional connectivity during working memory in schizophrenia. *Am. J. Psychiatry* **158**, 1809–1817 (2001).
3. S. Whitfield-Gabrieli, H. W. Thermenos, S. Milanovic, M. T. Tsuang, S. V. Faraone, R. W. McCarley, M. E. Shenton, A. I. Green, A. Nieto-Castanon, P. LaViolette, J. Wojcik, J. D. E. Gabrieli, L. J. Seidman, Hyperactivity and hyperconnectivity of the default network in schizophrenia and in first-degree relatives of persons with schizophrenia. *Proc. Natl. Acad. Sci. U.S.A.* **106**, 1279–1284 (2009).
4. G. Wu, L. Palaniyappan, M. Zhang, J. Yang, C. Xi, Z. Liu, Z. Xue, X. Ouyang, H. Tao, J. Zhang, Q. Luo, W. Pu, Imbalance between Prefronto-Thalamic and sensorimotor-thalamic circuitries associated with working memory deficit in Schizophrenia. *Schizophr. Bull.* **48**, 1–26 (2022).
5. H. Cao, X. Wei, N. Hu, W. Zhang, Y. Xiao, J. Zeng, J. A. Sweeney, R. Lencer, S. Lui, Q. Gong, Cerebello-Thalamo-Cortical hyperconnectivity classifies patients and predicts long-term treatment outcome in first-episode Schizophrenia. *Schizophr. Bull.* **48**, 505–513 (2021).
6. K. Supekar, L. Q. Uddin, A. Khouzam, J. Phillips, W. D. Gaillard, L. E. Kenworthy, B. E. Yerys, C. J. Vaidya, V. Menon, Brain hyper-connectivity in children with autism and its links to social deficits. *Cell Rep.* **5**, 738–747 (2013).
7. Brainstorm Consortium, V. Anttila, B. Bulik-Sullivan, H. K. Finucane, R. K. Walters, J. Bras, L. Duncan, V. Escott-Price, G. J. Falcone, P. Gormley, R. Malik, N. A. Patsopoulos, S. Ripke, Z. Wei, D. Yu, P. H. Lee, P. Turley, B. Grenier-Boley, V. Chouraki, Y. Kamatani, C. Berr, L. Letenneur, D. Hannequin, P. Amouyel, A. Boland, J.-F. Deleuze, E. Duron, B. N. Vardarajan, C. Reitz, A. M. Goate, M. J. Huentelman, M. I. Kamboh, E. B. Larson, E. Rogaeva, P. St. George-Hyslop, H. Hakonarson, W. A. Kukull, L. A. Farrer, L. L. Barnes, T. G. Beach, F. Y. Demirci, E. Head, C. M. Hulette, G. A. Jicha, J. S. K. Kauwe, J. A. Kaye, J. B. Leverenz, A. I. Levey, A. P. Lieberman, V. S. Pankratz, W. W. Poon, J. F. Quinn, A. J. Saykin, L. S. Schneider, A. G. Smith, J. A. Sonnen, R. A. Stern, V. M. Van Deerlin, L. J. Van Eldik, D. Harold, G. Russo, D. C. Rubinsztein, A. Bayer, M. Tsolaki, P. Proitsi, N. C. Fox, H. Hampel, M. J. Owen, S. Mead, P. Passmore, K. Morgan, M. M. Nöthen, M. Rossor, M. K. Lupton, P. Hoffmann, J. Kornhuber, B. Lawlor, A. M. Quillin, A. Al-Chalabi, J. C. Bis, A. Ruiz, M. Boada, S. Seshadri, A. Beiser, K. Rice, S. J. van der Lee, P. L. De Jager, D. H. Geschwind, M. Riemenschneider, S. Riedel-Heller, J. I. Rotter, G. Ransmayr, B. T. Hyman, C. Cruchaga, M. Alegret, B. Winsvold, P. Palta, K.-H. Farh, E. Cuenca-Leon, N. Furlotte, T. Kurth, L. Ligthart, G. M. Terwindt, T. Freilinger, C. Ran, S. D. Gordon, G. Borck, H. H. H. Adams, T. Lehtimäki, J. Wedenoja, J. E. Buring, M. Schürks,

M. Hrafnsdottir, J.-J. Hottenga, B. Penninx, V. Artto, M. Kaunisto, S. Vepsäläinen, N. G. Martin, G. W. Montgomery, M. I. Kurki, E. Hämäläinen, H. Huang, J. Huang, C. Sandor, C. Webber, B. Muller-Myhsok, S. Schreiber, V. Salomaa, E. Loehrer, H. Göbel, A. Macaya, P. Pozo-Rosich, T. Hansen, T. Werge, J. Kaprio, A. Metspalu, C. Kubisch, M. D. Ferrari, A. C. Belin, A. M. J. M. van den Maagdenberg, J.-A. Zwart, D. Boomsma, N. Eriksson, J. Olesen, D. I. Chasman, D. R. Nyholt, A. Avbersek, L. Baum, S. Berkovic, J. Bradfield, R. J. Buono, C. B. Catarino, P. Cossette, P. De Jonghe, C. Depondt, D. Dlugos, T. N. Ferraro, J. French, H. Hjalgrim, J. Jamnadas-Khoda, R. Kälviäinen, W. S. Kunz, H. Lerche, C. Leu, D. Lindhout, W. Lo, D. Lowenstein, M. M. Cormack, R. S. Møller, A. Molloy, P.-W. Ng, K. Oliver, M. Privitera, R. Radtke, A.-K. Ruppert, T. Sander, S. Schachter, C. Schankin, I. Scheffer, S. Schoch, S. M. Sisodiya, P. Smith, M. Sperling, P. Striano, R. Surges, G. N. Thomas, F. Visscher, C. D. Whelan, F. Zara, E. L. Heinzen, A. Marson, F. Becker, H. Stroink, F. Zimprich, T. Gasser, R. Gibbs, P. Heutink, M. Martinez, H. R. Morris, M. Sharma, M. Ryten, K. Y. Mok, S. Pulit, S. Bevan, E. Holliday, J. Attia, T. Battey, G. Boncoraglio, V. Thijs, W.-M. Chen, B. Mitchell, P. Rothwell, P. Sharma, C. Sudlow, A. Vicente, H. Markus, C. Kourkoulis, J. Pera, M. Raffeld, S. Silliman, V. B. Perica, L. M. Thornton, L. M. Huckins, N. W. Rayner, C. M. Lewis, M. Gratacos, F. Rybakowski, A. Keski-Rahkonen, A. Raevuori, J. I. Hudson, T. Reichborn-Kjennerud, P. Monteleone, A. Karwautz, K. Mannik, J. H. Baker, J. K. O'Toole, S. E. Trace, O. S. P. Davis, S. G. Helder, S. Ehrlich, B. Herpertz-Dahlmann, U. N. Danner, A. A. van Elburg, M. Clementi, M. Forzan, E. Docampo, J. Lissowska, J. Hauser, A. Tortorella, M. Maj, F. Gonidakis, K. Tziouvas, H. Papezova, Z. Yilmaz, G. Wagner, S. Cohen-Woods, S. Herms, A. Julià, R. Rabionet, D. M. Dick, S. Ripatti, O. A. Andreassen, T. Espeseth, A. J. Lundervold, V. M. Steen, D. Pinto, S. W. Scherer, H. Aschauer, A. Schosser, L. Alfredsson, L. Padyukov, K. A. Halmi, J. Mitchell, M. Strober, A. W. Bergen, W. Kaye, J. P. Szatkiewicz, B. Cormand, J. A. Ramos-Quiroga, C. Sánchez-Mora, M. Ribasés, M. Casas, A. Hervas, M. J. Arranz, J. Haavik, T. Zayats, S. Johansson, N. Williams, A. Dempfle, A. Rothenberger, J. Kuntsi, R. D. Oades, T. Banaschewski, B. Franke, J. K. Buitelaar, A. A. Vasquez, A. E. Doyle, A. Reif, K.-P. Lesch, C. Freitag, O. Rivero, H. Palmason, M. Romanos, K. Langley, M. Rietschel, S. H. Witt, S. Dalsgaard, A. D. Børglum, I. Waldman, B. Wilmot, N. Molly, C. H. D. Bau, J. Crosbie, R. Schachar, S. K. Loo, J. J. M. Gough, E. H. Grevet, S. E. Medland, E. Robinson, L. A. Weiss, E. Bacchelli, A. Bailey, V. Bal, A. Battaglia, C. Betancur, P. Bolton, R. Cantor, P. Celestino-Soper, G. Dawson, S. De Rubeis, F. Duque, A. Green, S. M. Klauck, M. Leboyer, P. Levitt, E. Maestrini, S. Mane, D. Moreno-De-Luca, J. Parr, R. Regan, A. Reichenberg, S. Sandin, J. Vorstman, T. Wassink, E. Wijsman, E. Cook, S. Santangelo, R. Delorme, B. Rogé, T. Magalhaes, D. Arking, T. G. Schulze, R. C. Thompson, J. Strohmaier, K. Matthews, I. Melle, D. Morris, D. Blackwood, A. M. Intosh, S. E. Bergen, M. Schalling, S. Jamain, A. Maaser, S. B. Fischer, C. S. Reinbold, J. M. Fullerton, J. Guzman-Parra, F. Mayoral, P. R. Schofield, S. Cichon, T. W. Mühleisen, F. Degenhardt, J. Schumacher, M. Bauer, P. B. Mitchell, E. S. Gershon, J. Rice, J. B. Potash, P. P. Zandi, N. Craddock, I. N. Ferrier, M. Alda, G. A. Rouleau, G. Turecki, R. Ophoff, C. Pato, A. Anjorin, E. Stahl, M. Leber, P. M. Czerski, C. Cruceanu, I. R. Jones, D. Posthuma, T. F. M. Andlauer, A. J. Forstner, F. Streit, B. T. Baune, T. Air, G. Sinnamon, N. R. Wray, D. J. M. Intyre, D. Porteous, G. Homuth, M. Rivera, J. Grove, C. M. Middeldorp, I. Hickie, M. Pergadia, D. Mehta, J. H. Smit, R. Jansen, E. de Geus, E. Dunn, Q. S. Li, M. Nauck, R. A. Schoevers, A. T. Beekman, J. A. Knowles, A. Viktorin, P. Arnold, C. L. Barr, G. Bedoya-Berrio, O. J. Bienvenu, H. Brentani, C. Burton, B. Camarena, C. Cappi, D. Cath, M. Cavallini, D. Cusi, S. Darrow, D. Denys, E. M. Derks, A. Dietrich, T. Fernandez, M. Figee, N. Freimer, G. Gerber, M. Grados, E. Greenberg, G. L. Hanna, A. Hartmann, M. E. Hirschtritt, P. J. Hoekstra, A. Huang, C. Huyser, C. Illmann, M. Jenike, S. Kuperman, B. Leventhal, C. Lochner, G. J. Lyon, F. Macciardi, M. Madruga-Garrido, I. A. Malaty, A. Maras, L. M. Grath, E. C. Miguel, P. Mir, G. Nestadt, H. Nicolini, M. S. Okun, A. Pakstis, P. Paschou, J. Piacentini, C. Pittenger, K. Plessen, V. Ramensky, E. M. Ramos, V. Reus, M. A. Richter, M. A. Riddle, M. M. Robertson, V. Roessner, M. Rosário, J. F. Samuels, P. Sandor, D. J. Stein, F. Tsetsos, F. Van Nieuwerburgh, S. Weatherall, J. R. Wendland, T. Wolanczyk, Y. Worbe, G. Zai, F. S. Goes, N. M. Laughlin, P. S. Nestadt, H.-J. Grabe, C. Depienne, A. Konkashbaev, N. Lanzagorta, A. Valencia-Duarte, E. Bramon, N. Buccola, W. Cahn, M. Cairns, S. A. Chong, D. Cohen, B. Crespo-Facorro, J. Crowley, M. Davidson, L. De Lisi, T. Dinan, G. Donohoe, E. Drapeau, J. Duan, L. Haan, D. Hougaard, S. Karachanak-Yankova, A. Khrunin, J. Klovins, V. Ku˘inskas, J. L. C. Keong, S. Limborska, C. Loughland, J. Lönnqvist, B. Maher, M. Mattheisen, C. M. Donald, K. C. Murphy, I. Nenadic, J. van Os, C. Pantelis, M. Pato, T. Petryshen, D. Quested, P. Roussos, A. R. Sanders, U. Schall, S. G. Schwab, K. Sim, H.-C. So, E. Stögmann, M. Subramaniam, D. Toncheva, J. Waddington, J. Walters, M. Weiser, W. Cheng, R. Cloninger, D. Curtis, P. V. Gejman, F. Henskens, M. Mattingsdal, S.-Y. Oh, R. Scott, B. Webb, G. Breen, C. Churchhouse, C. M. Bulik, M. Daly, M. Dichgans, S. V. Faraone, R. Guerreiro, P. Holmans, K. S. Kendler, B. Koeleman, C. A. Mathews, A. Price, J. Scharf, P. Sklar, J. Williams, N. W. Wood, C. Cotsapas, A. Palotie, J. W. Smoller, P. Sullivan, J. Rosand, A. Corvin, B. M. Neale, J. M. Schott, R. Anney, J. Elia, M. Grigoroiu-Serbanescu, H. J. Edenberg, R. Murray, Analysis of shared heritability in common disorders of the brain. *Science* **360**, eaap8757 (2018).

8. I. Kushima, B. Aleksic, M. Nakatochi, T. Shimamura, T. Okada, Y. Uno, M. Morikawa, K. Ishizuka, T. Shiino, H. Kimura, Y. Arioka, A. Yoshimi, Y. Takasaki, Y. Yu, Y. Nakamura, M. Yamamoto, T. Iidaka, S. Iritani, T. Inada, N. Ogawa, E. Shishido, Y. Torii, N. Kawano, Y. Omura, T. Yoshikawa, T. Uchiyama, T. Yamamoto, M. Ikeda, R. Hashimoto, H. Yamamori, Y. Yasuda, T. Someya, Y. Watanabe, J. Egawa, A. Nunokawa, M. Itokawa, M. Arai, M. Miyashita, A. Kobori, M. Suzuki, T. Takahashi, M. Usami, M. Kodaira, K. Watanabe, T. Sasaki, H. Kuwabara, M. Tochigi, F. Nishimura, H. Yamasue, Y. Eriguchi, S. Benner, M. Kojima, W. Yassin, T. Munesue, S. Yokoyama, R. Kimura, Y. Funabiki, H. Kosaka, M. Ishitobi, T. Ohmori, S. Numata, T. Yoshikawa, T. Toyota, K. Yamakawa, T. Suzuki, Y. Inoue, K. Nakaoka, Y. I. Goto, M. Inagaki, N. Hashimoto, I. Kusumi, S. Son, T. Murai, T. Ikegame, N. Okada, K. Kasai, S. Kunimoto, D. Mori, N. Iwata, N. Ozaki, Comparative analyses of copy-number variation in autism spectrum disorder and schizophrenia reveal etiological overlap and biological insights. *Cell Rep.* **24**, 2838–2856 (2018).

9. Cross-Disorder Group of the Psychiatric Genomics Consortium, Genomic relationships, novel loci, and pleiotropic mechanisms across eight psychiatric disorders. *Cell* **179**, 1469–1482.e11 (2019).

10. E. Rees, H. D. J. Creeth, H.-G. Hwu, W. J. Chen, M. Tsuang, S. J. Glatt, R. Rey, G. Kirov, J. T. R. Walters, P. Holmans, M. J. Owen, M. C. O'Donovan, Schizophrenia, autism spectrum disorders and developmental disorders share specific disruptive coding mutations. *Nat. Commun.* **12**, 5353 (2021).

11. T. Singh, T. Poterba, D. Curtis, H. Akil, M. al Eissa, J. D. Barchas, N. Bass, T. B. Bigdeli, G. Breen, E. J. Bromet, P. F. Buckley, W. E. Bunney, J. Bybjerg-Grauholm, W. F. Byerley, S. B. Chapman, W. J. Chen, C. Churchhouse, N. Craddock, C. M. Cusick, L. DeLisi, S. Dodge, M. A. Escamilla, S. Eskelinen, A. H. Fanous, S. V. Faraone, A. Fiorentino, L. Francioli, S. B. Gabriel, D. Gage, S. A. Gagliano Taliun, A. Ganna, G. Genovese, D. C. Glahn, J. Grove, M. H. Hall, E. Hämäläinen, H. O. Heyne, M. Holi, D. M. Hougaard, D. P. Howrigan, H. Huang, H. G. Hwu, R. S. Kahn, H. M. Kang, K. J. Karczewski, G. Kirov, J. A. Knowles, F. S. Lee, D. S. Lehrer, F. Lescai, D. Malaspina, S. R. Marder, S. A. McCarroll, A. M. McIntosh, H. Medeiros, L. Milani, C. P. Morley, D. W. Morris, P. B. Mortensen, R. M. Myers, M. Nordentoft, N. L. O'Brien, A. M. Olivares, D. Ongur, W. H. Ouwehand, D. S. Palmer, T. Paunio, D. Quested, M. H. Rapaport, E. Rees, B. Rollins, F. K. Satterstrom, A. Schatzberg, E. Scolnick, L. J. Scott, S. I. Sharp, P. Sklar, J. W. Smoller, J. L. Sobell, M. Solomonson, E. A. Stahl, C. R. Stevens, J. Suvisaari, G. Tiao, S. J. Watson, N. A. Watts, D. H. Blackwood, A. D. Børglum, B. M. Cohen, A. P. Corvin, T. Esko, N. B. Freimer, S. J. Glatt, C. M. Hultman, A. McQuillin, A. Palotie, C. N. Pato, M. T. Pato, A. E. Pulver, D. St. Clair, M. T. Tsuang, M. P. Vawter, J. T. Walters, T. M. Werge, R. A. Ophoff, P. F. Sullivan, M. J. Owen, M. Boehnke, M. C. O'Donovan, B. M. Neale, M. J. Daly, Rare coding variants in ten genes confer substantial risk for schizophrenia. *Nature* **604**, 509–516 (2022).

12. M. Fromer, A. J. Pocklington, D. H. Kavanagh, H. J. Williams, S. Dwyer, P. Gormley, L. Georgieva, E. Rees, P. Palta, D. M. Ruderfer, N. Carrera, I. Humphreys, J. S. Johnson, P. Roussos, D. D. Barker, E. Banks, V. Milanova, S. G. Grant, E. Hannon, S. A. Rose, K. Chambert, M. Mahajan, E. M. Scolnick, J. L. Moran, G. Kirov, A. Palotie, S. A. McCarroll, P. Holmans, P. Sklar, M. J. Owen, S. M. Purcell, M. C. O'Donovan, De novo mutations in schizophrenia implicate synaptic networks. *Nature* **506**, 179–184 (2014).

13. C. R. Marshall, D. P. Howrigan, D. Merico, B. Thiruvahindrapuram, W. Wu, D. S. Greer, D. Antaki, A. Shetty, P. A. Holmans, D. Pinto, M. Gujral, W. M. Brandler, D. Malhotra, Z. Wang, K. V. Fuentes Fajarado, M. S. Maile, S. Ripke, I. Agartz, M. Albus, M. Alexander, F. Amin, J. Atkins, S. A. Bacanu, R. A. Belliveau Jr., S. E. Bergen, M. Bertalan, E. Bevilacqua, T. B. Bigdeli, D. W. Black, R. Bruggeman, N. G. Buccola, R. L. Buckner, B. Bulik-Sullivan, W. Byerley, W. Cahn, G. Cai, M. J. Cairns, D. Campion, R. M. Cantor, V. J. Carr, N. Carrera, S. V. Catts, K. D. Chambert, W. Cheng, C. R. Cloninger, D. Cohen, P. Cormican, N. Craddock, B. Crespo-Facorro, J. J. Crowley, D. Curtis, M. Davidson, K. L. Davis, F. Degenhardt, J. D. Favero, L. E. De Lisi, D. Dikeos, T. Dinan, S. Djurovic, G. Donohoe, E. Drapeau, J. Duan, F. Dudbridge, P. Eichhammer, J. Eriksson, V. Escott-Price, L. Essioux, A. H. Fanous, K.-H. Farh, M. S. Farrell, J. Frank, L. Franke, R. Freedman, N. B. Freimer, J. I. Friedman, A. J. Forstner, M. Fromer, G. Genovese, L. Georgieva, E. S. Gershon, I. Giegling, P. Giusti-Rodríguez, S. Godard, J. I. Goldstein, J. Gratten, L. de Haan, M. L. Hamshere, M. Hansen, T. Hansen, V. Haroutunian, A. M. Hartmann, F. A. Henskens, S. Herms, J. N. Hirschhorn, P. Hoffmann, A. Hofman, H. Huang, M. Ikeda, I. Joa, A. K. Kähler, R. S. Kahn, L. Kalaydjieva, J. Karjalainen, D. Kavanagh, M. C. Keller, B. J. Kelly, J. L. Kennedy, Y. Kim, J. A. Knowles, B. Konte, C. Laurent, P. Lee, S. H. Lee, S. E. Legge, B. Lerer, D. L. Levy, K.-Y. Liang, J. Lieberman, J. Lönnqvist, C. M. Loughland, P. K. E. Magnusson, B. S. Maher, W. Maier, J. Mallet, M. Mattheisen, M. Mattingsdal, R. W. McCarley, C. M. Donald, A. M. McIntosh, S. Meier, C. J. Meijer, I. Melle, R. I. Mesholam-Gately, A. Metspalu, P. T. Michie, L. Milani, V. Milanova, Y. Mokrab, D. W. Morris, B. Müller-Myhsok, K. C. Murphy, R. M. Murray, I. Myin-Germeys, I. Nenadic, D. A. Nertney, G. Nestadt, K. K. Nicodemus, L. Nisenbaum, A. Nordin, E. O'Callaghan, C. O'Dushlaine, S.-Y. Oh, A. Olincy, L. Olsen, F. A. O'Neill, J. Van Os, C. Pantelis, G. N. Papadimitriou, E. Parkhomenko, M. T. Pato, T. Paunio, Psychosis Endophenotypes International Consortium, D. O. Perkins, T. H. Pers, O. Pietiläinen, J. Pimm, A. J. Pocklington, J. Powell, A. Price, A. E. Pulver, S. M. Purcell, D. Quested, H. B. Rasmussen, A. Reichenberg, M. A. Reimers, A. L. Richards, J. L. Roffman, P. Roussos, D. M. Ruderfer, V. Salomaa, A. R. Sanders, A. Savitz, U. Schall, T. G. Schulze, S. G. Schwab, E. M. Scolnick, R. J. Scott, L. J. Seidman, J. Shi, J. M. Silverman, J. W. Smoller, E. Söderman, C. C. A. Spencer, E. A. Stahl, E. Strengman, J. Strohmaier, T. S. Stroup, J. Suvisaari, D. M. Svrakic, J. P. Szatkiewicz, S. Thirumalai, P. A. Tooney, J. Veijola, P. M. Visscher, J. Waddington, D. Walsh, B. T. Webb, M. Weiser, D. B. Wildenauer, N. M. Williams, S. Williams, S. H. Witt, A. R. Wolen, B. K. Wormley,

N. R. Wray, J. Q. Wu, C. C. Zai, R. Adolfsson, O. A. Andreassen, D. H. R. Blackwood, E. Bramon, J. D. Buxbaum, S. Cichon, D. A. Collier, A. Corvin, M. J. Daly, A. Darvasi, E. Domenici, T. Esko, P. V. Gejman, M. Gill, H. Gurling, C. M. Hultman, N. Iwata, A. V. Jablensky, E. G. Jönsson, K. S. Kendler, G. Kirov, J. Knight, D. F. Levinson, Q. S. Li, S. A. M. Carroll, A. M. Quillin, J. L. Moran, B. J. Mowry, M. M. Nöthen, R. A. Ophoff, M. J. Owen, A. Palotie, C. N. Pato, T. L. Petryshen, D. Posthuma, M. Rietschel, B. P. Riley, D. Rujescu, P. Sklar, D. S. Clair, J. T. R. Walters, T. Werge, P. F. Sullivan, M. C. O'Donovan, S. W. Scherer, B. M. Neale, J. Sebat, CNV, Schizophrenia Working Groups of the Psychiatric Genomics Consortium, Contribution of copy number variants to schizophrenia from a genome-wide study of 41,321 subjects. *Nat. Genet.* **49**, 27–35 (2017).

14. D. P. Howrigan, S. A. Rose, K. E. Samocha, M. Fromer, F. Cerrato, W. J. Chen, C. Churchhouse, K. Chambert, S. D. Chandler, M. J. Daly, A. Dumont, G. Genovese, H. G. Hwu, N. Laird, J. A. Kosmicki, J. L. Moran, C. Roe, T. Singh, S. H. Wang, S. V. Faraone, S. J. Glatt, S. A. McCarroll, M. Tsuang, B. M. Neale, Exome sequencing in schizophrenia-affected parent-offspring trios reveals risk conferred by protein-coding de novo mutations. *Nat. Neurosci.* **23**, 185–193 (2020).
15. A. Hayashi-Takagi, Synapse pathology and translational applications for schizophrenia. *Neurosci. Res.* **114**, 3–8 (2017).
16. Y. Sztainberg, H. Y. Zoghbi, Lessons learned from studying syndromic autism spectrum disorders. *Nat. Neurosci.* **19**, 1408–1417 (2016).
17. R. Yuste, Dendritic spines and distributed circuits. *Neuron* **71**, 772–781 (2011).
18. A. Holtmaat, K. Svoboda, Experience-dependent structural synaptic plasticity in the mammalian brain. *Nat. Rev. Neurosci.* **10**, 647–658 (2009).
19. M. L. MacDonald, J. Alhassan, J. T. Newman, M. Richard, H. Gu, R. M. Kelly, A. R. Sampson, K. N. Fish, P. Penzes, Z. P. Wills, D. A. Lewis, R. A. Sweet, Selective loss of smaller spines in schizophrenia. *Am. J. Psychiatry* **174**, 586–594 (2017).
20. T. Singh, M. I. Kurki, D. Curtis, S. M. Purcell, L. Crooks, J. M. Rae, J. Suvisaari, H. Chheda, D. Blackwood, G. Breen, O. Pietiläinen, S. S. Gerety, M. Ayub, M. Blyth, T. Cole, D. Collier, E. L. Coomber, N. Craddock, M. J. Daly, J. Danesh, M. D. Forti, A. Foster, N. B. Freimer, D. Geschwind, M. Johnstone, S. Joss, G. Kirov, J. Körkkö, O. Kuismin, P. Holmans, C. M. Hultman, C. Iyegbe, J. Lönnqvist, M. Männikkö, S. A. M. Carroll, P. M. Guffin, A. M. M. Intosh, A. M. Quillin, J. S. Moilanen, C. Moore, R. M. Murray, R. Newbury-Ecob, W. Ouwehand, T. Paunio, E. Prigmore, E. Rees, D. Roberts, J. Sambrook, P. Sklar, D. S. Clair, J. Veijola, J. T. R. Walters, H. Williams; Swedish Schizophrenia Study; INTERVAL Study; DDD Study; UK10 K Consortium, P. F. Sullivan, M. E. Hurles, M. C. O'Donovan, A. Palotie, M. J. Owen, J. C. Barrett, Rare loss-of-function variants in SETD1A are associated with schizophrenia and developmental disorders. *Nat. Neurosci.* **19**, 571–577 (2016).
21. J. K. Millar, J. C. Wilson-Annan, S. Anderson, S. Christie, M. S. Taylor, C. A. Semple, R. S. Devon, D. M. St Clair, W. J. Muir, D. H. Blackwood, D. J. Porteous, Disruption of two novel genes by a translocation co-segregating with schizophrenia. *Hum. Mol. Genet.* **9**, 1415–1423 (2000).
22. T. N. Turner, F. Hormozdiari, M. H. Duyzend, S. A. McClymont, P. W. Hook, I. Iossifov, A. Raja, C. Baker, K. Hoekzema, H. A. Stessman, M. C. Zody, B. J. Nelson, J. Huddleston, R. Sandstrom, J. D. Smith, D. Hanna, J. M. Swanson, E. M. Faustman, M. J. Bamshad, J. Stamatoyannopoulos, D. A. Nickerson, A. S. McCallion, R. Darnell, E. E. Eichler, Genome sequencing of autism-affected families reveals disruption of putative noncoding regulatory DNA. *Am. J. Hum. Genet.* **98**, 58–74 (2016).
23. K. Nagahama, K. Sakoori, T. Watanabe, Y. Kishi, K. Kawaji, M. Koebis, K. Nakao, Y. Gotoh, A. Aiba, N. Uesaka, M. Kano, Setd1a insufficiency in mice attenuates excitatory synaptic function and recapitulates schizophrenia-related behavioral abnormalities. *Cell Rep.* **32**, 108126 (2020).
24. A. Hayashi-Takagi, M. Takaki, N. Graziane, S. Seshadri, H. Murdoch, A. J. Dunlop, Y. Makino, A. J. Seshadri, K. Ishizuka, D. P. Srivastava, Z. Xie, J. M. Baraban, M. D. Houslay, T. Tomoda, N. J. Brandon, A. Kamiya, Z. Yan, P. Penzes, A. Sawa, Disrupted-in-Schizophrenia 1 (DISC1) regulates spines of the glutamate synapse via Rac1. *Nat. Neurosci.* **13**, 327–332 (2010).
25. A. Hayashi-Takagi, Y. Araki, M. Nakamura, B. Vollrath, S. G. Duron, Z. Yan, H. Kasai, R. L. Huganir, D. A. Campbell, A. Sawa, PAKs inhibitors ameliorate schizophrenia-associated dendritic spine deterioration in vitro and in vivo during late adolescence. *Proc. Natl. Acad. Sci. U.S.A.* **111**, 6461–6466 (2014).
26. M. Matsuzaki, G. C. R. Ellis-Davies, T. Nemoto, Y. Miyashita, M. Iino, H. Kasai, Dendritic spine geometry is critical for AMPA receptor expression in hippocampal CA1 pyramidal neurons. *Nat. Neurosci.* **4**, 1086–1092 (2001).
27. M. L. Hines, N. T. Carnevale, The NEURON simulation environment. *Neural Comput.* **9**, 1179–1209 (1997).
28. A. Hayashi-Takagi, S. Yagishita, M. Nakamura, F. Shirai, Y. I. Wu, A. L. Loshbaugh, B. Kuhlman, K. M. Hahn, H. Kasai, Labelling and optical erasure of synaptic memory traces in the motor cortex. *Nature* **525**, 333–338 (2015).
29. M. Trommald, V. Jensen, P. Andersen, Analysis of dendritic spines in rat CA1 pyramidal cells intracellularly filled with a fluorescent dye. *J. Comp. Neurol.* **353**, 260–274 (1995).
30. K. Kuroda, S. Yamada, M. Tanaka, M. Iizuka, H. Yano, D. Mori, D. Tsuboi, T. Nishioka, T. Namba, Y. Iizuka, S. Kubota, T. Nagai, D. Ibi, R. Wang, A. Enomoto, M. Isotani-Sakakibara, N. Asai, K. Kimura, H. Kiyonari, T. Abe, A. Mizoguchi, M. Sokabe, M. Takahashi, K. Yamada, K. Kaibuchi, Behavioral alterations associated with targeted disruption of exons 2 and 3 of the Disc1 gene in the mouse. *Hum. Mol. Genet.* **20**, 4666–4683 (2011).
31. A. Polsky, B. W. Mel, J. Schiller, Computational subunits in thin dendrites of pyramidal cells. *Nat. Neurosci.* **7**, 621–627 (2004).
32. T. Branco, B. A. Clark, M. Hausser, Dendritic discrimination of temporal input sequences in cortical neurons. *Science* **329**, 1671–1675 (2010).
33. J. Schiller, Y. Schiller, G. Stuart, B. Sakmann, Calcium action potentials restricted to distal apical dendrites of rat neocortical pyramidal neurons. *J. Physiol.* **505**, 605–616 (1997).
34. S. Funahashi, C. J. Bruce, P. S. Goldman-Rakic, Mnemonic coding of visual space in the monkey's dorsolateral prefrontal cortex. *J. Neurophysiol.* **61**, 331–349 (1989).
35. A. Compte, N. Brunel, P. S. Goldman-Rakic, X. J. Wang, Synaptic mechanisms and network dynamics underlying spatial working memory in a cortical network model. *Cereb. Cortex* **10**, 910–923 (2000).
36. T. Okimura, S. Tanaka, T. Maeda, M. Kato, M. Mimura, Simulation of the capacity and precision of working memory in the hypodopaminergic state: Relevance to schizophrenia. *Neuroscience* **295**, 80–89 (2015).
37. P. J. Harrison, The neuropathology of schizophrenia. A critical review of the data and their interpretation. *Brain* **122**, 593–624 (1999).
38. R. N. Moda-Sava, M. H. Murdock, P. K. Parekh, R. N. Fetcho, B. S. Huang, T. N. Huynh, J. Witztum, D. C. Shaver, D. L. Rosenthal, E. J. Alway, K. Lopez, Y. Meng, L. Nellissen, L. Grosenick, T. A. Milner, K. Deisseroth, H. Bito, H. Kasai, C. Liston, Sustained rescue of prefrontal circuit dysfunction by antidepressant-induced spine formation. *Science* **364**, eaat8078 (2019).
39. A. Takata, I. Ionita-Laza, J. A. Gogos, B. Xu, M. Karayiorgou, De novo synonymous mutations in regulatory elements contribute to the genetic etiology of autism and schizophrenia. *Neuron* **89**, 940–947 (2016).
40. N. J. Brandon, A. Sawa, Linking neurodevelopmental and synaptic theories of mental illness through DISC1. *Nat. Rev. Neurosci.* **12**, 707–722 (2011).
41. S. E. McCarthy, J. Gillis, M. Kramer, J. Lihm, S. Yoon, Y. Berstein, M. Mistry, P. Pavlidis, R. Solomon, E. Ghiban, E. Antoniou, E. Kelleher, C. O'Brien, G. Donohoe, M. Gill, D. W. Morris, W. R. McCombie, A. Corvin, De novo mutations in schizophrenia implicate chromatin remodeling and support a genetic overlap with autism and intellectual disability. *Mol. Psychiatry* **19**, 652–658 (2014).
42. S. De Rubeis, X. He, A. P. Goldberg, C. S. Poultney, K. Samocha, A. E. Cicek, Y. Kou, L. Liu, M. Fromer, S. Walker, T. Singh, L. Klei, J. Kosmicki, F. Shih-Chen, B. Aleksic, M. Biscaldi, P. F. Bolton, J. M. Brownfeld, J. Cai, N. G. Campbell, A. Carracedo, M. H. Chahrour, A. G. Chiocchetti, H. Coon, E. L. Crawford, S. R. Curran, G. Dawson, E. Duketis, B. A. Fernandez, L. Gallagher, E. Geller, S. J. Guter, R. S. Hill, J. Ionita-Laza, P. J. Gonzalez, H. Kilpinen, S. M. Klauck, A. Kolevzon, I. Lee, I. Lei, J. Lei, T. Lehtimäki, C.-F. Lin, A. Ma'ayan, C. R. Marshall, A. L. M. Innes, B. Neale, M. J. Owen, N. Ozaki, M. Parellada, J. R. Parr, S. Purcell, K. Puura, D. Rajagopalan, K. Rehnström, A. Reichenberg, A. Sabo, M. Sachse, S. J. Sanders, C. Schafer, M. Schulte-Rüther, D. Skuse, C. Stevens, P. Szatmari, K. Tammimies, O. Valladares, A. Voran, W. Li-San, L. A. Weiss, A. J. Willsey, T. W. Yu, R. K. C. Yuen; DDD Study; Homozygosity Mapping Collaborative for Autism; UK10K Consortium; Autism Sequencing Consortium, E. H. Cook, C. M. Freitag, M. Gill, C. M. Hultman, T. Lehner, A. Palotie, G. D. Schellenberg, P. Sklar, M. W. State, J. S. Sutcliffe, C. A. Walsh, S. W. Scherer, M. E. Zwick, J. C. Barett, D. J. Cutler, K. Roeder, B. Devlin, M. J. Daly, J. D. Buxbaum, Synaptic, transcriptional and chromatin genes disrupted in autism. *Nature* **515**, 209–215 (2014).
43. P. Penzes, M. E. Cahill, K. A. Jones, J. E. VanLeeuwen, K. M. Woolfrey, Dendritic spine pathology in neuropsychiatric disorders. *Nat. Neurosci.* **14**, 285–293 (2011).
44. D. A. Lewis, A. A. Curley, J. R. Glausier, D. W. Volk, Cortical parvalbumin interneurons and cognitive dysfunction in schizophrenia. *Trends Neurosci.* **35**, 57–67 (2012).
45. N. S. Desai, J. J. Siegel, W. Taylor, R. A. Chitwood, D. Johnston, MATLAB-based automated patch-clamp system for awake behaving mice. *J. Neurophysiol.* **114**, 1331–1345 (2015).
46. G. Major, M. E. Larkum, J. Schiller, Active properties of neocortical pyramidal neuron dendrites. *Annu. Rev. Neurosci.* **36**, 1–24 (2013).
47. G. J. Stuart, N. Spruston, Dendritic integration: 60 years of progress. *Nat. Neurosci.* **18**, 1713–1721 (2015).
48. J. P. Hamm, Y. Shymkiv, J. Mukai, J. A. Gogos, R. Yuste, Aberrant cortical ensembles and schizophrenia-like sensory phenotypes in *Setd1a*$^{+/-}$ Mice. *Biol. Psychiatry* **88**, 215–223 (2020).
49. M. T. Ke, Y. Nakai, S. Fujimoto, R. Takayama, S. Yoshida, T. S. Kitajima, M. Sato, T. Imai, Super-resolution mapping of neuronal circuitry with an index-optimized clearing agent. *Cell Rep.* **14**, 2718–2732 (2016).
50. H. Okazaki, A. Hayashi-Takagi, A. Nagaoka, M. Negishi, H. Ucar, S. Yagishita, K. Ishii, T. Toyoizumi, K. Fox, H. Kasai, Calcineurin knockout mice show a selective loss of small spines. *Neurosci. Lett.* **671**, 99–102 (2018).

51. A. R. Mohn, R. R. Gainetdinov, M. G. Caron, B. H. Koller, Mice with reduced NMDA receptor expression display behaviors related to schizophrenia. *Cell* **98**, 427–436 (1999).
52. H. Zeng, S. Chattarji, M. Barbarosie, L. Rondi-Reig, B. D. Philpot, T. Miyakawa, M. F. Bear, S. Tonegawa, Forebrain-specific calcineurin knockout selectively impairs bidirectional synaptic plasticity and working/episodic-like memory. *Cell* **107**, 617–629 (2001).
53. H. T. Ito, S. E. Smith, E. Hsiao, P. H. Patterson, Maternal immune activation alters nonspatial information processing in the hippocampus of the adult offspring. *Brain Behav. Immun.* **24**, 930–941 (2010).
54. R. C. Paolicelli, G. Bolasco, F. Pagani, L. Maggi, M. Scianni, P. Panzanelli, M. Giustetto, T. A. Ferreira, E. Guiducci, L. Dumas, D. Ragozzino, C. T. Gross, Synaptic pruning by microglia is necessary for normal brain development. *Science* **333**, 1456–1458 (2011).
55. Y. M. Morizawa, M. Matsumoto, Y. Nakashima, N. Endo, T. Aida, H. Ishikane, K. Beppu, S. Moritoh, H. Inada, N. Osumi, E. Shigetomi, S. Koizumi, G. Yang, H. Hirai, K. Tanaka, K. F. Tanaka, N. Ohno, Y. Fukazawa, K. Matsui, Synaptic pruning through glial synapse engulfment upon motor learning. *Nat. Neurosci.* **25**, 1458–1469 (2022).
56. J. Schindelin, I. Arganda-Carreras, E. Frise, V. Kaynig, M. Longair, T. Pietzsch, S. Preibisch, C. Rueden, S. Saalfeld, B. Schmid, J. Y. Tinevez, D. J. White, V. Hartenstein, K. Eliceiri, P. Tomancak, A. Cardona, Fiji: An open-source platform for biological-image analysis. *Nat. Methods* **9**, 676–682 (2012).
57. K. Diba, C. Koch, I. Segev, Spike propagation in dendrites with stochastic ion channels. *J. Comput. Neurosci.* **20**, 77–84 (2006).
58. A. Polsky, B. Mel, J. Schiller, Encoding and decoding bursts by NMDA spikes in basal dendrites of layer 5 pyramidal neurons. *J. Neurosci.* **29**, 11891–11903 (2009).

Acknowledgments: We thank F. Shirai, T. McHugh, S. Tsutsumi, V. Sekulic, M. Murayama, T. Toyoizumi, and L. Kusmierz for invaluable discussions and N. Koibuchi for supervision of Graduate Education. We thank Y. Hisano, E. Ebisui, T. Maegawa, and M. Matsumoto for experimental supports. **Funding:** This research was supported by Grants-in-Aid from the Ministry of Education, Culture, Sports, Science, and Technology (MEXT, Japan: 17H05735, 18H05428, and 18H05433 to A.H.-T.; 17K07068 to N.S.; 19H05204 and 21H04785 to M.K.; 18H05120 and 19H03323 to Y.F.); AMED (JP22wm0525021 to A.H.-T.); NIH grants (MH071533 and MH116046 to R.A.S.); and the Support Unit for Bio-Material Analysis, Research Resource Division, RIKEN Center for Brain Science. **Author contributions:** K.O.-N. and N.S. performed electrophysiological recordings, morphological analysis, single-cell computations, and human postmortem brain analysis. K.O.-N. and R.M. performed behavioral experiments. K.O.-N. and K.O. performed in vivo imaging. K.N. and M.K. generated the *SETD1A* hKO mice. T.O. and S.T. performed computations. Y.F. performed EM experiment. M.L.M., K.N.F., and R.A.S. provided the imaging dataset of postmortem SZ brains. K.O.-N. and A.H.-T. designed the study. A.H.-T. wrote the manuscript. **Competing interests:** The authors declare that they have no competing interests. **Data and materials availability:** All data needed to evaluate the conclusions in the paper are present in the paper and/or the Supplementary Materials. The detailed code of NEURON simulation is available in ModelDB (http://modeldb.yale.edu/266844). The dataset for postmortem brain imaging can be provided by R.A.S. pending scientific review and a completed collaboration data transfer agreement. *DISC*1 LoF mice (no. CDB0583K) can be provided by the RIKEN BRC through the National BioResource Project for the MEXT/AMED, Japan. *SETD1A* hKO can be provided pending a completed material transfer agreement with M.K.

Submitted 26 August 2022
Accepted 5 May 2023
Published 9 June 2023
10.1126/sciadv.ade5973

ScienceAdvances

Distorted neurocomputation by a small number of extra-large spines in psychiatric disorders

Kisho Obi-Nagata, Norimitsu Suzuki, Ryuhei Miyake, Matthew L. MacDonald, Kenneth N. Fish, Katsuya Ozawa, Kenichiro Nagahama, Tsukasa Okimura, Shoji Tanaka, Masanobu Kano, Yugo Fukazawa, Robert A. Sweet, and Akiko Hayashi-Takagi

Sci. Adv. **9** (23), eade5973. DOI: 10.1126/sciadv.ade5973

Science Advances (ISSN 2375-2548) is published by the American Association for the Advancement of Science. 1200 New York Avenue NW, Washington, DC 20005. The title *Science Advances* is a registered trademark of AAAS.